

# Ice Cloud Retrievals and Analysis with the Compact Scanning Submillimeter Imaging Radiometer and the Cloud Radar System during CRYSTAL-FACE <sup>1</sup>

**K. Franklin Evans<sup>2</sup>**

Program in Atmospheric and Oceanic Sciences, University of Colorado  
Boulder, Colorado

**James R. Wang, Paul E. Racette, Gerald Heymsfield, and Lihua Li**

NASA Goddard Spaceflight Center  
Greenbelt, Maryland

March 15, 2004

<sup>1</sup>To be submitted to the Journal of Applied Meteorology

<sup>2</sup>*Corresponding author address:* Dr. K. Franklin Evans, University of Colorado, 311 UCB, Boulder, 80309-0311. Email: evans@nit.colorado.edu

## Abstract

# 1. Introduction

There are currently no methods for accurate global remote sensing of ice cloud mass for climate studies (Wielicki et al., 1995). Global measurements of vertically integrated cloud ice mass (ice water path or IWP) are important for evaluating climate model parameterizations and studying the upper tropospheric water budget. Visible and infrared satellite remote sensing techniques for ice clouds (e.g. Rossow and Schiffer, 1999; Stubenrauch et al., 1999) have poor accuracy for high IWP clouds, which contain much of the total cloud ice mass. Thermal infrared methods saturate for moderate optical depth and can only determine particle size (and hence IWP) for effective radius below about  $50 \mu\text{m}$ . Solar reflection methods can't distinguish ice from water cloud optical depth, can't measure thinner clouds over bright surfaces, and retrieve particle sizes near cloud top for optically thicker clouds, which results in biased IWP retrievals. Millimeter-wave radar backscattering from CloudSat (Stephens et al., 2002), when combined with visible reflectance measurements, will improve IWP retrieval accuracy, but the radar's nadir view provides coverage that is too sparse to obtain a global climatology of cloud ice mass.

Theoretical studies (Gasiewski, 1992; Evans and Stephens, 1995b; Evans et al., 1998) have suggested that millimeter-wave and submillimeter-wave radiometry has the potential for accurate retrievals of cloud IWP and characteristic ice particle size. The technology of submillimeter-wave radiometry has lagged the theory, and only recently have the first submillimeter measurements of ice clouds been made from aircraft. The Far InfraRed Sensor for Cirrus (FIRSC), which is a Fourier Transform Spectrometer with a cryogenic bolometer detector (Vanek et al., 2001), made measurements to above 1000 GHz during several campaigns. Since FIRSC's bolometric detector has low sensitivity, however, the brightness temperature noise is high below about 800 GHz and cross-track scanning is precluded. The Submillimeter-Wave Cloud Ice Radiometer developed at the Jet Propulsion Laboratory (Evans et al., 2002) has heterodyne receivers at 183, 325, 448, and 643 GHz, but has not yet been flown. The Millimeter-wave Imaging Radiometer (MIR) (Racette et al., 1996) had receivers at 89, 150, 183, and 220 GHz. Several groups have developed cloud IWP retrieval algorithms for MIR data at 89, 150, and 220 GHz (Liu and Curry, 2000; Deeter and Evans, 2000; Weng and Grody, 2000). A 340 GHz channel was later added to MIR, and significant brightness temperature depressions were observed from Arctic cirrus (Wang et al., 2001).

The Compact Scanning Submillimeter Imaging Radiometer (CoSSIR) is a new instrument with 12 channels from 183 to 640 GHz. CoSSIR flew for the first time on the NASA ER-2 aircraft during the CRYSTAL-FACE deployment out of Key West, Florida in July 2002. The 94 GHz nadir viewing Cloud Radar System (CRS) flew with CoSSIR on the ER-2. In this paper we describe CoSSIR and show examples of millimeter-wave and submillimeter-wave brightness temperature depressions associated with convective anvils in the south Florida region. We describe using a Bayesian algorithm, with updated prior information on ice cloud microphysics, to retrieve ice water path and median volume equivalent sphere diameter ( $D_{me}$ ). Retrievals from CoSSIR of integrated radar reflectivity are compared with CRS data to evaluate the CoSSIR retrievals. Lastly, a new algorithm is developed to retrieve profiles of ice water content (IWC) and  $D_{me}$  from the combination of CoSSIR and CRS data.

## 2. Data

During the month of July 2002, a major field campaign, the Cirrus Regional Study of Tropical Anvils and Cirrus Layers – Florida Area Cirrus Experiment (CRYSTAL-FACE), was conducted by NASA over the region surrounding Florida. Five aircraft equipped with a variety of remote sensing instruments and in-situ probes participated in this campaign; all of these aircraft were stationed in Key West, Florida. The NASA ER-2 aircraft was one of the five and was equipped with a suite of highly sophisticated remote sensors including the CoSSIR and the 94 GHz Cloud Radar System (CRS) (Li et al., 2003) that measures radar reflectivity profiles of cloud particles. CoSSIR is a new, total-power radiometer that has 9 horizontally polarized channels at the frequencies of  $183.3\pm 1.0$ ,  $183.3\pm 3.0$ ,  $183.3\pm 6.6$ , 220,  $380.2\pm 0.8$ ,  $380.2\pm 1.8$ ,  $380.2\pm 3.3$ ,  $380.2\pm 6.2$ , and 640 GHz, and 3 vertically polarized channels at  $487.25\pm 0.8$ ,  $487.25\pm 1.2$ ,  $487.25\pm 3.3$  (see Table 1 below). It can be programmed to perform across-track scans as well as conical scans at a fixed incidence angle. During CRYSTAL-FACE it was programmed in across-track scan mode so that coincident measurements with the CRS could be made. The 3 dB beamwidth is about 4 degrees and is frequency independent; at the ER-2 aircraft cruising altitude of about 20 km, the footprint at a typical ice cloud altitude of 10 km is 600 m. [Jim: there should be a discussion of the calibration method and expected accuracy].

Table 1 below gives a comparison of the calculated and measured  $NE\Delta T$  for all the working channels; the  $380.2\pm 0.8$  GHz channel did not function during the entire deployment. Clearly the measured values of  $NE\Delta T$  are 2 to 10 times higher than the calculated values. Examination of the CoSSIR throughput reveals that the analog to digital conversion contributed a significant fraction of the radiometer noise. A modification to the signal conditioning and digitization technique is required to eliminate this noise source and improve the sensor performance.

Table 2 lists a summary of the CoSSIR flights for this deployment. There were a total of 11 science flights in Florida and two transit flights between NASA Dryden Flight Research Center at Edwards Air Base, California and Key West, Florida in July 2002. CoSSIR experienced a motion control problem for six science flights from July 9 through 23, which was resolved by adjusting the gain of the motion control feedback. Towards the end of the tenth science flight on July 28, the pilot inadvertently turned off the power to CoSSIR before decent and the whole system was cold-soaked after landing. Only the four lowest frequency channels (183.3 and 220 GHz) and the 640 GHz channel remained operational after this incident. The calibrated CoSSIR data sets along nadir were placed in the CRYSTAL-FACE archive (at <http://espoarchive.nasa.gov/>). [Jim: Should there be a description of the processing/data editing technique that you used?] The imagery data sets are deemed too large for archival; they will be made available by contacting one of us (e.g., James.R.Wang@nasa.gov).

The CRS is a new instrument operating at 94 GHz frequency that was built and first flown in CRYSTAL-FACE. It is a Doppler, polarimetric radar developed for autonomous operation on the ER-2 aircraft and ground operation (Li et al., 2003). Its antenna beamwidth and gain are  $0.6^\circ\times 0.7^\circ$  and 46.4 dB, respectively. It has a noise figure of 7.5 dB and its receiver bandwidth can be varied between 1, 2, and 4 MHz. The system transmits power in either vertical (V) or horizontal (H) polarization, and receives backscatter power in both V and H polarization at the nadir direction. The dataset used here has a measured sen-

Table 1: CoSSIR channel characteristics.

Channel (GHz)	Center Frequency (GHz)	Bandwidth (GHz)	System Temperature (K)	NE $\Delta$ T <sup>1</sup> (calculated) (K)	NE $\Delta$ T <sup>2</sup> (measured) (K)
183.3±1.0	1.0	0.5	2500	0.55	0.90
183.3±3.0	3.0	1.0	1390	0.23	0.61
183.3±6.6	6.6	1.5	1050	0.15	0.75
220	2.5	3.0	1760	0.16	0.84
380.2±0.8	0.75	0.7	3460	0.63	NA
380.2±1.8	1.80	1.0	8440	1.23	4.01
380.2±3.3	3.35	1.7	4820	0.55	4.25
380.2±6.2	6.20	3.6	6670	0.52	4.99
487.25±0.8	0.68	0.35	4650	1.17	2.57
487.25±1.2	1.19	0.48	3890	0.85	1.66
487.25±3.3	3.04	2.93	4600	0.40	2.05
640	2.5	3.0	16000	1.33	4.90

<sup>1</sup>Calculated values based on receiver system temperature measured in the laboratory and 50 msec integration time. <sup>2</sup>Measured from the flight data with the same integration time.

Table 2: Summary of science flights during CRYSTAL-FACE (2002).

Flight	Date	Status	Receivers working
Transit	July 1	Successful	183.3, 220, 380, 487 and 640 GHz
1	July 3	Successful	183.3, 220, 380, and 640 GHz
2	July 7	Successful	183.3, 220, 380, and 640 GHz
3	July 9	Failed	
4	July 11	Failed	
5	July 13	Failed	
6	July 16	Failed	
7	July 19	Failed	
8	July 23	Failed	
9	July 26	Successful	183.3, 220, 380, and 640 GHz
10	July 28	Successful	183.3, 220, 380, and 640 GHz
11	July 29	Successful	183.3, 220, and 640 GHz
Transit	July 30	Successful	183.3, 220, and 640 GHz

sitivity of -29 dBZ at 10 km range, 150 m range resolution, and 1 second averaging. The calibration of the CRS was conducted by two different methods. The first one was an inter-comparison of the concurrent measurements for similar cloud volumes between the CRS and the ground-based 95 GHz Cloud Profiling Radar System (CPRS) owned by the University of Massachusetts (Sekelsky and McIntosh, 1996) and well maintained and calibrated over the past decade. This comparison demonstrated consistency between the two instruments to better than 1 dB Li et al. (2003). The second method was to use the ocean surface (Durden et al., 1994) by estimating scattering cross section of the surface return  $\sigma_0$  at a low incidence angle and with quasi-specular scattering theory Valenzuela (1978). The ER-2 aircraft dropsondes provided temperature, pressure, relative humidity, and near-surface wind conditions that were required to take into account the effect of atmospheric absorption water vapor and oxygen, as well as the calculations of  $\sigma_0$ . The analysis showed that the calculated  $\sigma_0$  agreed with the other CRS calibration results. The details of the system descriptions, sensitivity, and calibration can be found in Li et al. (2003). The CRS successfully collected scientific data from all the flights listed in Table 2, except for July 7.

Figures 1, 2, and 3 provide a glimpse of data acquired by the CoSSIR and CRS during CRYSTAL-FACE. Figure 1 shows an example of pseudo-color image of brightness temperatures ( $T_b$ ) for several selected CoSSIR channels from a segment of a transit flight from NASA Dryden Flight Research Center to Key West, Florida on July 1, 2002. The swath of each image is about 45 km across at the ground (much less for high clouds) and the segment covers a distance of about 600 km. Two strong cells of ice clouds can be found near the times of 1952 UTC and 2010 UTC; a weak cell is also spotted 2032 UTC. These cells clearly demonstrate that ice clouds strongly scatter submillimeter-wave radiation and that the  $T_b$  depressions are generally larger at higher frequencies. Notice that the effect of water vapor absorption causes a large range in the  $T_b$  values from the three 183.3 GHz channels.

Figure 2 gives a comparison of the along-nadir  $T_b$  values from some selected CoSSIR channels with the concurrent radar reflectivity profiles  $Z_e$  measured by the CRS. The time interval of the plot covers about the top half of the images in Figure 1. The two large  $T_b$  depressions near 1952 UTC and 2010 UTC identified with the ice clouds from the  $T_b$  images in Figure 1 are clearly associated with the high CRS  $Z_e$  values. The  $T_b$  depression from the isolated high cloud around 2006 UTC is much greater at 640 GHz than 220 GHz. Another smaller 640 GHz  $T_b$  depression near 2015 UTC not apparent in Figure 1 finds its correspondence in CRS  $Z_e$  profile as well. Additionally, the higher-frequency channels generally show  $T_b$  depressions over a greater distance than the lower frequency channels. For example, the  $T_b$  values around 1958 UTC from the  $183.3 \pm 6.6$  and 220 GHz channels are already recovered to their clear sky values, while those from the 640 GHz channel remain slightly depressed due to the presence of high clouds detected by the CRS. This clearly demonstrates the increased sensitivity of the 640 GHz channel to high and thin clouds.

Another important feature displayed by the CoSSIR data is the non-linear behavior of the  $T_b$  relation between high and low frequencies, shown by the scatter plot in Fig. 3 for the 640 and 220 GHz channels. In the higher  $T_b$  range with small depressions, the 640 GHz  $T_b$  decrease is steeper than the 220 GHz decrease, implying a higher sensitivity of 640 GHz to thinner ice clouds. This higher sensitivity of the higher frequency implies clouds with a smaller median mass diameter ( $D_{me}$ ) particles (see Figure 3 of Wang et al. (1998)). In the lower  $T_b$  range corresponding to larger depressions, the 640 GHz depression is less than that

CosSIR Imagery  
CRYSTAL-FACE Campaign - 07/01/2002  
19:48:10 -> 20:43:10 UTC

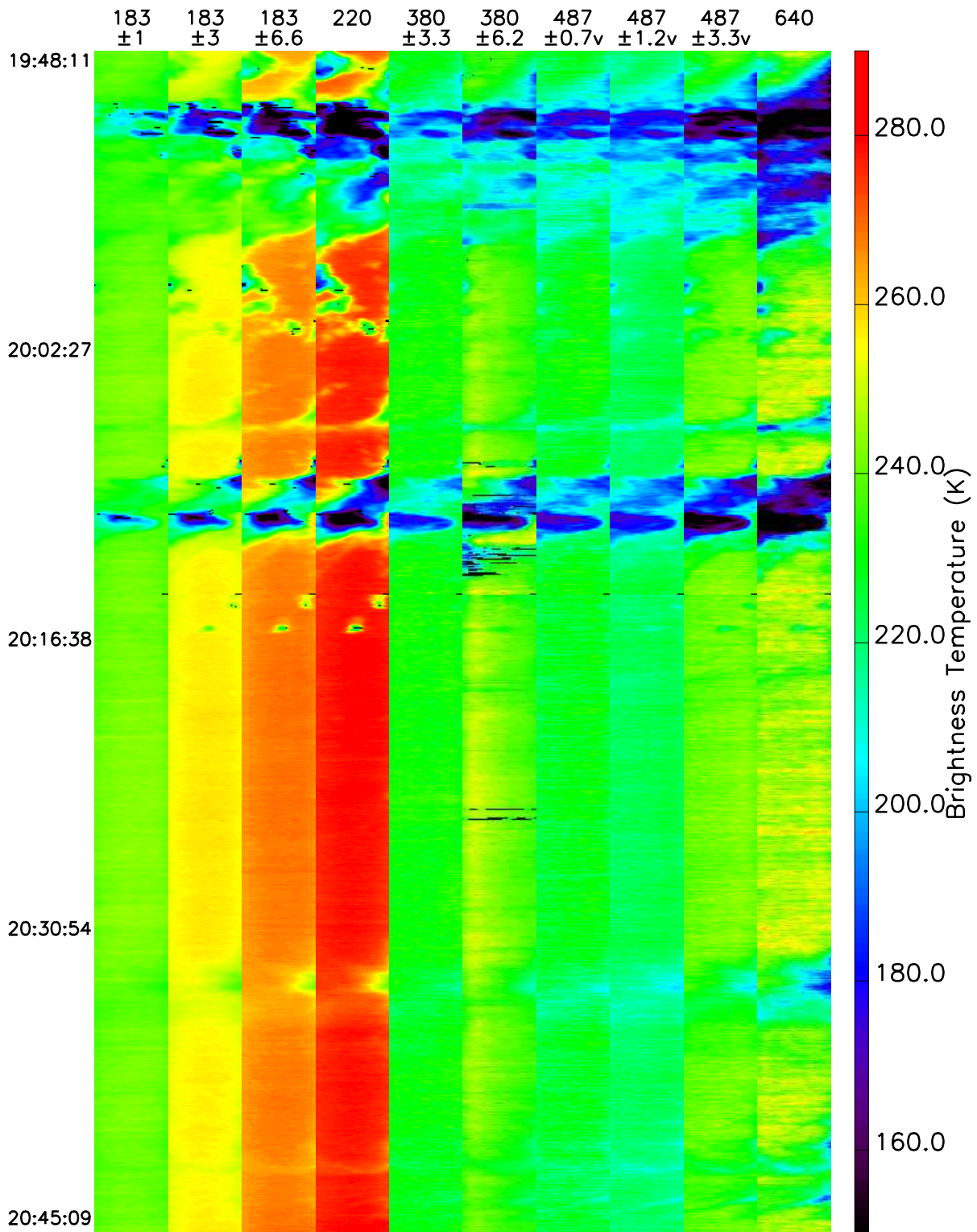


Figure 1: Example brightness temperature images from 10 of CoSSIR's channels.

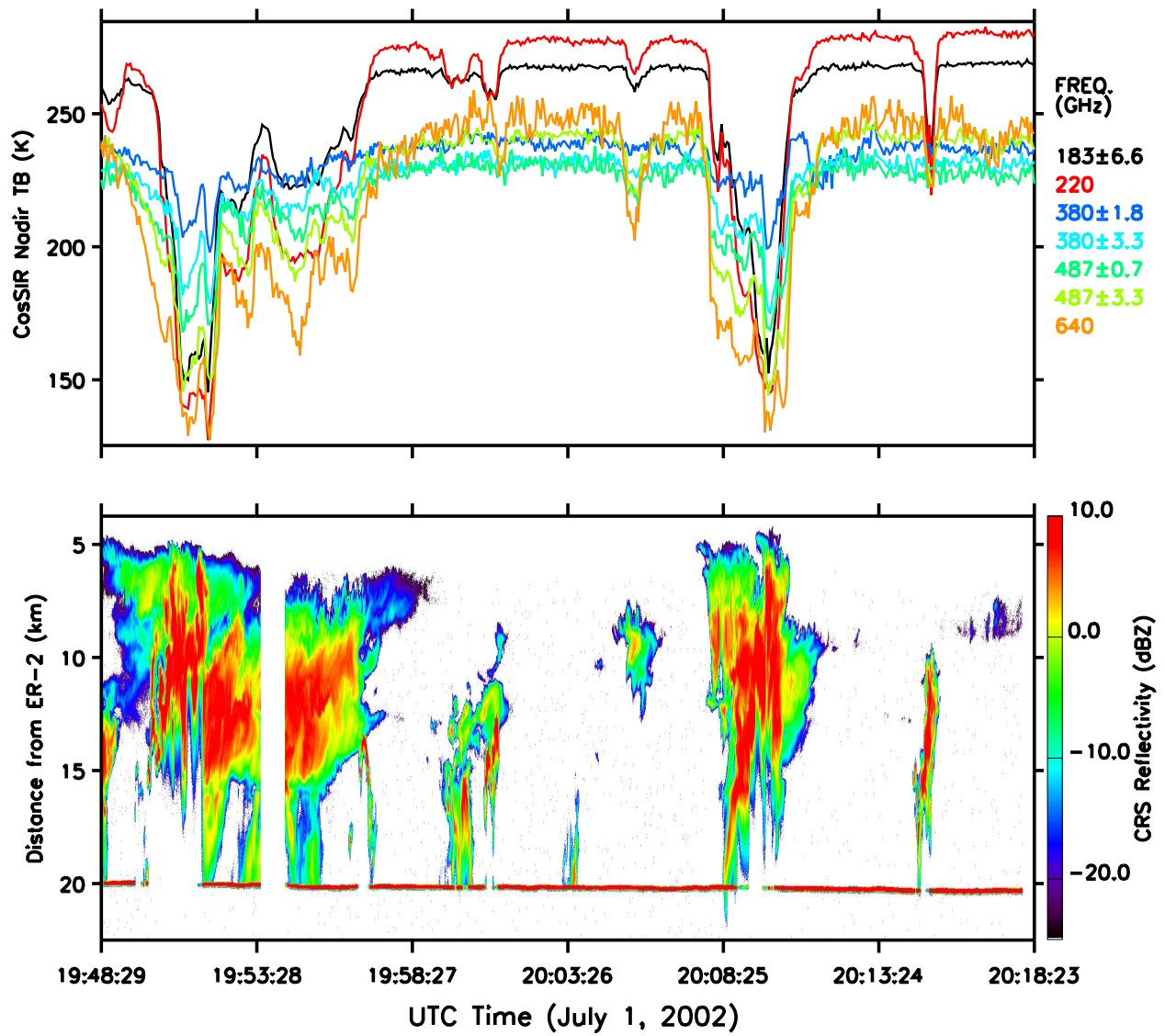


Figure 2: Nadir CoSSIR brightness temperatures and corresponding CRS radar reflectivity.

at 220 GHz, implying larger  $D_{me}$  and generally thick clouds over regions of precipitation. The small population of points below the slanted line are from times when the 640 GHz  $T_b$ s were drifting unphysically. The points inside the ellipse are from lower altitude ice clouds (as verified by CRS data), for which the water vapor absorption reduces the  $T_b$  depression at 640 GHz.

### 3. Vertically integrated ice cloud retrieval algorithm

A Monte Carlo Bayesian integration algorithm (Evans et al., 2002) is used to retrieve ice cloud IWP and  $D_{me}$  from the CoSSIR brightness temperatures. The Monte Carlo integration

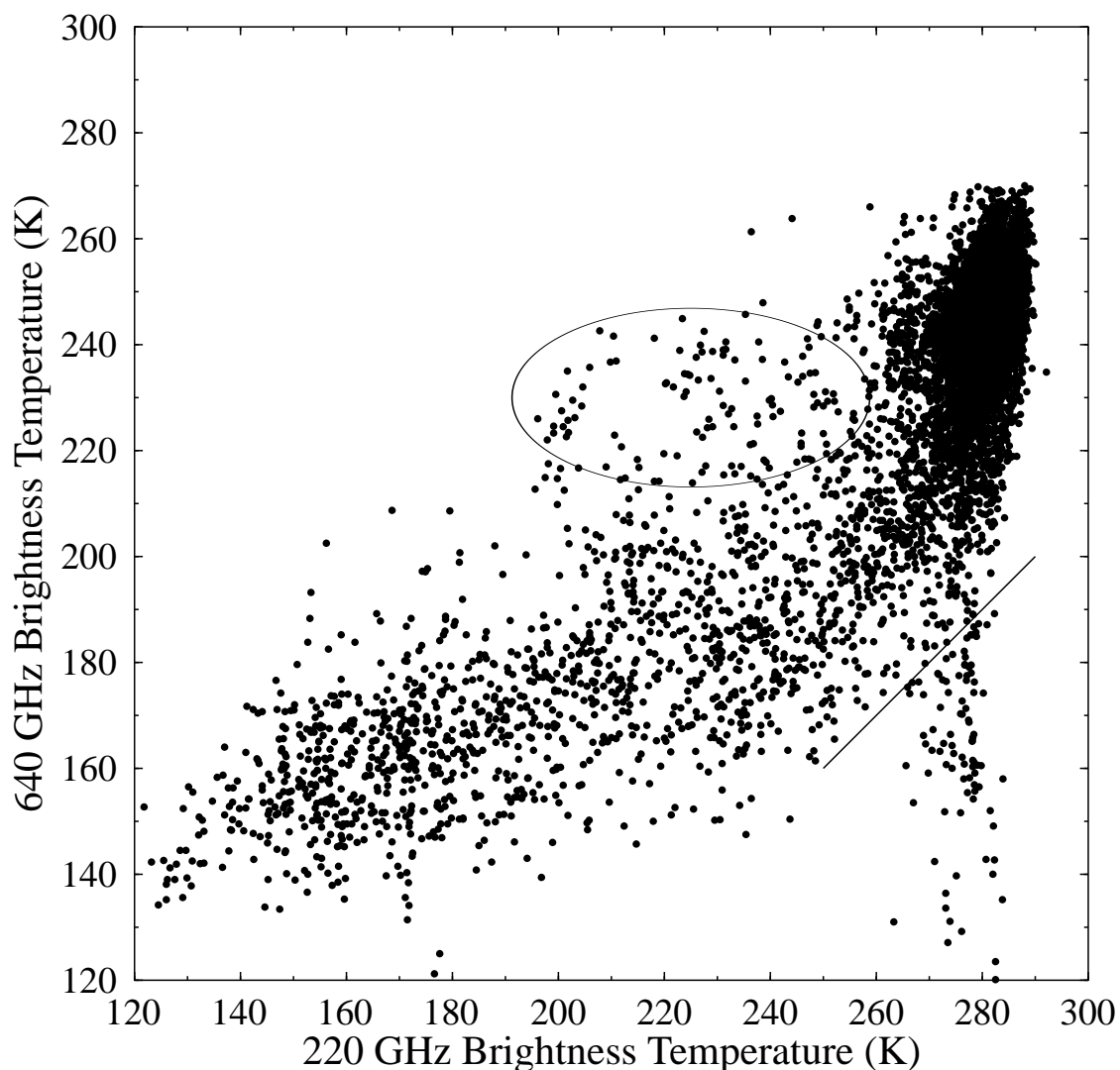


Figure 3: Scatterplot of nadir CoSSIR 640 and 220 GHz brightness temperatures from July 3, 28, and 29.

is over state vectors  $\mathbf{x}_i$  of cloud and atmosphere parameters. A priori information on the temperature and water vapor profile and ice cloud geometry and microphysics is introduced by distributing the vectors randomly according to a prior probability density function (pdf),  $p_p(\mathbf{x})$ . A radiative transfer model simulates CoSSIR brightness temperatures  $T_{sim,j}$  (for the  $j$ 'th channel) from the cloud and atmosphere profile represented by  $\mathbf{x}_i$ . A retrieval for the CoSSIR observed brightness temperatures,  $T_{obs,j}$ , having rms errors of  $\sigma_j$ , is performed by computing the mean state vector over the posterior pdf from Bayes theorem. Assuming a normally distributed likelihood function for the observations given the state vector, the retrieved state is

$$\mathbf{x}_{ret} = \frac{\sum_i \mathbf{x}_i \exp\left[-\frac{1}{2}\chi_i^2\right]}{\sum_i \exp\left[-\frac{1}{2}\chi_i^2\right]} \quad \mathbf{x}_i \text{ from } p_p(\mathbf{x}) \quad (1)$$

where  $\chi^2$  is the usual normalized measure of the disagreement between the observed and simulated brightness temperature vectors,

$$\chi_i^2 = \sum_{j=1}^M \frac{[T_{obs,j} - T_{sim,j}(\mathbf{x}_i)]^2}{\sigma_j^2} \quad (2)$$

A similar summation gives the standard deviation around the mean vector, which is an estimate of the uncertainty in the retrieval. For efficiency the simulated brightness temperatures for each Monte Carlo vector ( $\mathbf{x}_i$ ) are precomputed with a radiative transfer model and stored with the desired retrieval parameters (e.g. IWP and  $D_{me}$ ) in a file called the retrieval database. The database used here has  $10^6$  cases in it.

Several minor improvements have been made to the Bayesian ice cloud retrieval algorithm described in Evans et al. (2002). Missing channels are dealt with by simply setting that channel's  $\sigma_j$  to 1000 times the normal value and using the mean channel value for  $T_{obs,j}$ . The algorithm requires a minimum number of database points (25 in the retrievals below) within a specified  $\chi^2$  threshold, here set to  $M + 4\sqrt{M}$ , where  $M$  is the number of channels in the retrieval. This choice of the  $\chi^2$  threshold is guided by noting that for Gaussian measurement noise and  $M \gg 1$ , the expected value of  $\chi^2$  is  $M$  and the standard deviation of  $\chi^2$  is  $\sqrt{2M}$ . If there are fewer than the required number of points within this threshold due to the finite number of points in the retrieval database, then a larger  $\chi^2$  range is considered by effectively increasing all the  $\sigma_j$ 's in steps of a factor of  $\sqrt{2}$  until the minimum number of points is reached. This implies that there is a source of retrieval error due to the finite database size. Since the points in the database are distributed according to the prior pdf, there are few cases with high IWP. The database generation procedure has the option of rejecting low IWP cases according to an exponential probability distribution in IWP and increasing the weight of the remaining cases so that the high IWP enriched retrieval database is statistically equivalent to the prior pdf. This procedure improves the problem of not having enough database points within the required  $\chi^2$  threshold for higher IWP.

Generation of the database of atmospheric parameters and corresponding brightness temperatures is the key element of the Bayesian algorithm. The first step in generating the database is to create random profiles of temperature, water vapor, liquid and ice cloud properties, and surface emissivity. The distribution of these parameters is the a priori information in the retrieval, so it is important that the profiles are realistic and completely cover the possible parameter range.

The retrieval database temperature and relative humidity profiles are generated with appropriate statistics and vertical correlations using principal component analysis. The principal components are calculated from 25 radiosonde profiles on July 3, 7, 9, 21, 28, 29 obtained from the Miami National Weather Service and the PNNL Atmospheric Remote Sensing Laboratory (PARSL) at the west coast ground site. Twenty principal components, which explain 99.8% of the variance in temperature and relative humidity, are used. Heights above the highest radiosonde level and the fixed ozone profile are obtained from a standard tropical atmosphere. The mean relative humidity profile in the generation process (not the output stochastic profile) is set to ice saturation for the cloudy levels.

This retrieval database is made with single layer clouds, which may be ice, mixed phase, or even pure liquid depending (stochastically) on temperature. The cloud geometry statistics are obtained from over 1400 cloudy CRS profiles on four flights, where the thickest cloud layer with top height above 9.5 km is chosen from each profile. The top height is Gaussian distributed with a mean of 12.7 km and standard deviation of 1.2 km. The cloud thickness is exponentially distributed with a mean of 5.0 km.

The new mixed phase procedure first decides whether the cloud is a pure water or ice cloud. The probability of a cloud being a pure water cloud depends linearly on the cloud top temperature between two specified temperature values (248 K to 268 K used here) and is 0 below and 1 above the range. The probability of a cloud being a pure ice cloud depends linearly on the cloud base temperature between two temperature values (253 K to 273 K used here). If a cloud is not a pure water cloud, and is not a pure ice cloud, then it is mixed phase. The mass fraction of water depend linearly on height within the cloud according to random water fractions chosen for the cloud top and base. The water fraction at cloud top and base is a triangular distribution with halfwidth of 0.25, and the mean varies linearly in height with a value of 0 at the level of homogeneous freezing (-39°C) and a value of 1 at the melting level. The water fraction is set to 0 above the homogeneous freezing level and 1 below the melting level. The total water content at cloud top and base is derived from the ice microphysics statistics. The liquid droplet median mass diameter is normally distributed (uniform within a cloud) with a mean of 18  $\mu\text{m}$  and standard deviation of 4  $\mu\text{m}$ .

The microphysical properties of the ice clouds in the retrieval database are based on CRYSTAL-FACE data from in situ cloud probes on the Citation aircraft. The results of this analysis (described in appendix A) are the joint statistics of temperature, IWC, and  $D_{me}$  as summarized by the mean vector and covariance matrix of temperature,  $\ln(\text{IWC})$ , and  $\ln(D_{me})$ . The randomly generated ice cloud heights and thicknesses are used to index into the random temperature profiles to get cloud top and bottom temperatures. Given the top and bottom temperature, the IWC and  $D_{me}$  at the top and bottom of the cloud are generated randomly from the bivariate log-normal distribution. The  $D_{me}$  varies linearly with height inside the cloud, while the IWC varies as a power law in  $D_{me}$ . The bottom IWC and  $D_{me}$  are required to be larger than cloud top values.

Ice particle shape and size distribution width are error sources in the ice cloud retrievals. The construction of random aggregate particles based loosely on Cloud Particle Imager pictures and the simulation of CoSSIR and CRS scattering properties for size distributions of these particles is described in appendix B. For each cloud a single particle shape is selected from the five modeled shapes (low-density spherical snow, aggregates of frozen droplets, two varieties of aggregates of hexagonal plates, and aggregates of plates and hexagonal columns).

The width of the ice particle gamma distribution is also randomly chosen for each cloud from three widths.

The surface has a small contribution at 220 GHz for the drier stochastic atmospheres (the 220 GHz transmission for the mean atmosphere is only 4.4%). Even the driest atmospheres have essentially no transmission at the other CoSSIR frequencies. The surface emissivity is Gaussian distributed with a mean of 0.93 and a standard deviation of 0.03. The surface temperature is obtained from the random atmosphere temperature at zero height.

The second part of generating the retrieval database is to simulate the CoSSIR and CRS observations with a radiative transfer model. A fast Eddington second approximation method is used. The microwave radiances are simulated for a nadir viewing angle. For efficiency the monochromatic absorption profiles for an input atmosphere are interpolated in temperature and water vapor from reference profiles calculated with LBLRTM version 8.3. Double sideband brightness temperatures are calculated with two monochromatic radiative transfer computations. The tabulated single scattering properties for the ice particles are computed as described in appendix B.

In addition to the simulated CoSSIR brightness temperatures, the retrieval database has two simulated 94 GHz CRS observables: integrated backscattering ( $I_b$ ) and the mean backscattering weighted height ( $z_b$ ). The integrated backscattering is defined by

$$I_b = \int_{z_1}^{z_2} \frac{\sigma_{back}(z)}{4\pi} dz = \int_{z_1}^{z_2} \frac{\sigma_{sca} P(180^\circ)}{4\pi} dz, \quad (3)$$

where  $\sigma_{back}(z)$  is the volume backscattering coefficient,  $\sigma_{sca}$  is the volume scattering coefficient,  $P(180^\circ)$  is the phase function evaluated for the backscattering coefficient, and  $z_1$  to  $z_2$  is the height range. The height ranged used here is 4.5 to 17 km, or all cloudy levels above the freezing level. Although not in common use in radar meteorology, integrated backscattering is a natural measure in radiative transfer and is used in lidar remote sensing. The units of integrated backscattering are  $\text{ster}^{-1}$ . The radar observables in the database are used 1) to retrieve  $I_b$  from CoSSIR data to compare with CRS data, and 2) to perform IWP and  $D_{me}$  retrievals with the combination of CoSSIR and CRS data.

#### 4. CoSSIR and CRS vertically integrated ice cloud retrievals and analysis

To perform the Bayesian ice cloud retrievals from CoSSIR measurements, the rms uncertainties ( $\sigma_j$ ) must be determined for each channel during each flight. Only the nadir viewing CoSSIR brightness temperatures for roll angles less than  $8^\circ$  are used. The “noise” of the CoSSIR  $T_b$ s are determined by calculating the standard deviation for clear sky segments of the flights. Clear sky is defined as those pixels for which the MODIS Airborne Simulator (MAS)  $11.0 \mu\text{m}$  brightness temperature is above 295 K. This method for estimating the  $\sigma$ 's assumes most of the variability is instrumental, not due to water vapor variability, which is certainly true for the channels above 220 GHz. The variability estimate is probably high for the 183 GHz and 220 GHz channels. The actual  $\sigma$  used is chosen somewhat subjectively between the standard deviations for short time segments and those for the whole flight. The channels and  $\sigma$ 's used in the retrievals are listed in Table 3 for each flight. The  $\sigma$ 's for the

183 GHz and 220 GHz channels are kept fixed, while those for the other channels varies with the flight. To minimize the error due to uncertainties in the exact local oscillator frequency for the 380 and 487 GHz receivers, we use only the channel with the bandpass farthest from the central frequency.

The evaluation of CoSSIR IWP and  $D_{me}$  retrievals is carried out by comparing integrated reflectivity retrieved from CoSSIR with that calculated from the CRS data. This indirect approach avoids the large errors in retrieving IWP and  $D_{me}$  from radar reflectivity profiles. The CRS data are relatively independent of the CoSSIR  $T_b$ 's, since the CRS reflectivity is backscattering and at a considerably lower frequency. Figure 4 illustrates this idea of independent physics by comparing the sensitivity of CRS reflectivity and CoSSIR brightness temperature depressions to particle size for a fixed ice water content. An exponent near zero means that the measurement is related to IWP with little dependence on  $D_{me}$ . For smaller particles the CRS reflectivity is in the Rayleigh regime, where  $n = 3$ , but the exponent decreases for larger particles as 94 GHz enters the Mie regime. The large difference in the  $D_{me}$  exponents between the CRS and various CoSSIR channels implies that the CRS and CoSSIR are independent measurements over most of the range in  $D_{me}$ .

The comparison of CoSSIR retrievals with CRS data is limited to flights on July 3, 28, and 29. The CRS data is unavailable on July 7, and the CoSSIR retrievals for July 1 and 30 are only strictly valid for the end or the beginning of the flights when the ER-2 was in the south Florida vicinity (the prior information on the atmospheric profile and perhaps the microphysics is expected to change with location). For comparison with CoSSIR retrievals and to use in combined retrievals, the CRS data is vertically averaged and converted to integrated backscattering using

$$I_b = \int \frac{\pi^4 |K_w|^2}{4\lambda^4} Z_e dz = (1.653 \times 10^{-7} \text{ m}^2/\text{mm}^6) \int Z_e dz, \quad (4)$$

where  $|K_w|^2 = 0.6975$ ,  $\lambda = 0.3184$  cm is the wavelength,  $Z_e$  is the CRS equivalent radar reflectivity factor, and the integration is from 4.5 km to 17 km. The integrated backscattering (with units of  $\text{ster}^{-1}$ ) is converted to dB. As an example, a 10 km deep cloud with a CRS reflectivity of 10 dBZ has an integrated backscattering of -17.8 dB. The mean and standard deviation of integrated backscattering for no echo conditions is -58.5 dB and 2.75 dB, re-

Table 3: CoSSIR channels and brightness temperature uncertainties ( $\sigma_j$ , K) used in retrievals.

Day	Channels (GHz)						
	183.3±1.0	183.3±3.0	183.3±6.6	220.0	380.2±6.2	487.2±3.0	640
1	2.0	2.0	2.0	1.5	8.0	7.0	7.0
3	2.0	2.0	2.0	1.5	10.0	–	6.0
7	2.0	2.0	2.0	1.5	10.0	–	16.0
28	2.0	2.0	2.0	1.5	7.0	–	10.0
29	2.0	2.0	2.0	1.5	–	–	12.0
30	2.0	2.0	2.0	1.5	–	–	12.0

Particle Size Sensitivity:  $Z_e \propto (\text{IWC}) D_{me}^n$  or  $\Delta T_b \propto (\text{IWP}) D_{me}^n$

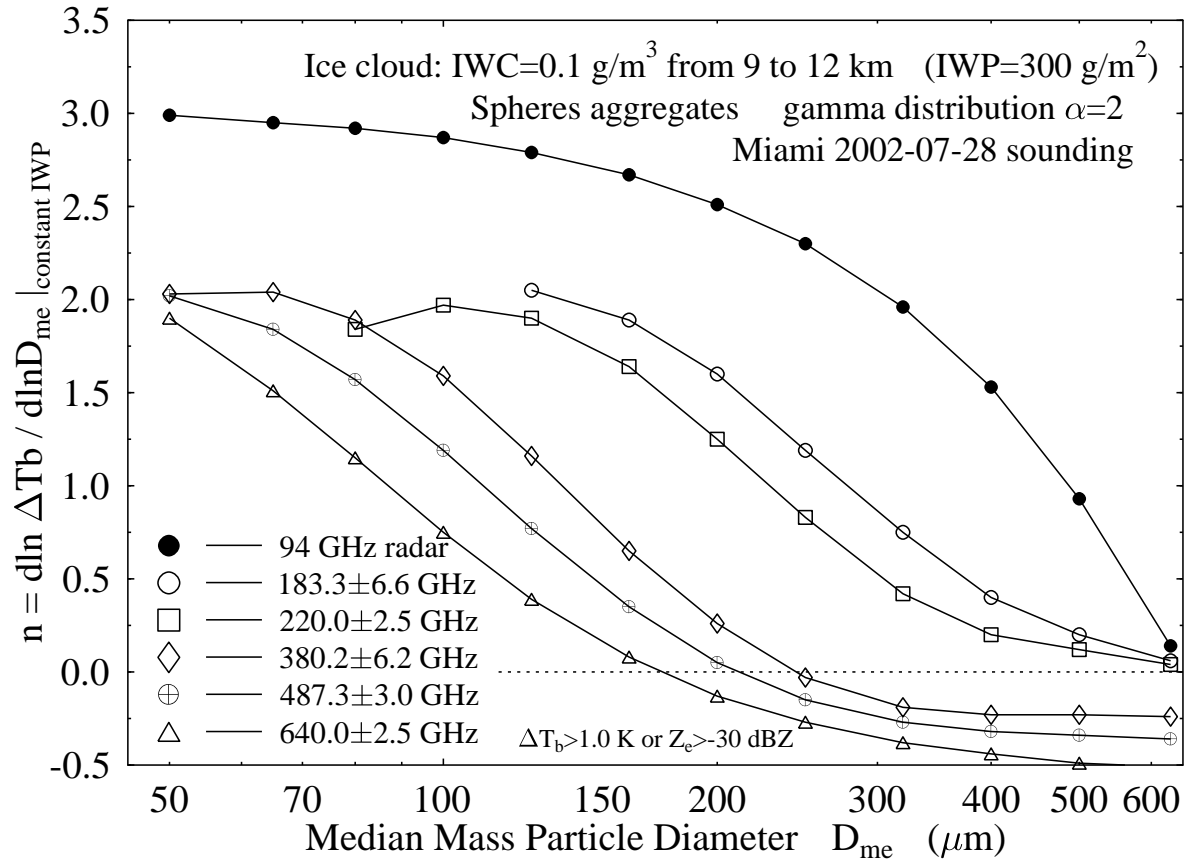


Figure 4: Theoretical calculations comparing the sensitivity to particle size ( $D_{me}$ ) for constant ice water content (IWC) of 94 GHz radar reflectivity ( $Z_e$ ) and CoSSIR brightness temperature depressions ( $\Delta T_b$ ).

spectively. Therefore -50 dB is taken as the threshold for using integrated backscattering data in the analysis below.

Figures 5 to 7 show examples of CoSSIR IWP and  $D_{me}$  retrievals and comparison of CoSSIR retrieved and CRS integrated backscattering. The IWP ranges up to over 10,000 g/m<sup>2</sup> for the thickest parts of the anvils. The retrieved IWP error is approximately equal to the IWP for IWP below about 200 g/m<sup>2</sup>. The reason for the poor sensitivity to low IWP is the high noise on the more sensitive submillimeter channels (380 and 640 GHz; see Table 3). The retrieved  $D_{me}$  ranges from 500 to 600  $\mu$ m in the thickest regions to around 200  $\mu$ m (though with large error bars) in the thin anvil regions. There is remarkable agreement between the retrieved and CRS integrated backscattering in the thick anvil regions, though the retrievals are a few dB high in the July 3 example. The retrieved integrated backscattering error bars are also very small for the deep anvils. In the thinner regions the integrated backscattering error bars increase substantially, and thus the retrievals still agree statistically with the CRS data.

Statistics comparing the retrieved and CRS integrated backscattering are shown in Fig. 8 for the 1027, 1050, and 1225 retrievals on July 3, 28, and 29, respectively. For all three flights the median differences are above 3 dB for integrated backscattering below -30 dB. For the July 28 and 29 flights the differences drop to 1 dB or below for the highest integrated backscattering (-20 to -10 dB), but the retrieval error for the July 3 flight is larger. In addition to the CoSSIR retrieval using the channels listed in Table 3, the integrated backscattering error statistics are also shown for retrievals using just the three 183 GHz and one 220 GHz channels. Eliminating the submillimeter channels slightly degrades the thinner region retrievals on July 28, but dramatically *improves* the thinner region retrievals on July 3. This may indicate that the submillimeter channels were malfunctioning on July 3 or that the CoSSIR  $T_b$  errors are underestimated. The lack of a significant improvement in the integrated backscattering retrieval error for thinner anvil regions with the addition of the submillimeter channels is another indication that those channels were too noisy to add much value to the low noise millimeter-wave channels. The normalized differences shown in Fig. 8 are the median of the absolute value of the integrated backscattering differences divided by the retrieved error bars. That the normalized differences are about unity or less, except for the thick regions on July 3, suggests that the Bayesian error bars are reasonably estimated and that there are no large systematic errors in the retrievals.

Besides using the CRS integrated backscattering to evaluate the CoSSIR retrievals, it can also be input to the Bayesian retrieval algorithm. In this case, there is no longer any validation, but it is still useful to see how the IWP and  $D_{me}$  retrievals, and especially the error bars, behave. In addition to the integrated backscattering, the backscattering weighted cloud height is input to the Bayesian algorithm. The calibration uncertainty ( $\sigma$ ) in CRS integrated backscattering used for the retrieval is 1.0 dB, and the  $\sigma$  for the weighted cloud height is taken to be 0.5 km (so as to not unnecessarily restrict the number of matching database cases). The retrieval results for July 28 are presented here statistically in Fig. 9, which shows the median retrieved IWP and  $D_{me}$  as a function of integrated backscattering for CRS only, CoSSIR only, and CRS + CoSSIR retrievals. Overall, the retrievals for the three instrument configurations are fairly similar. In the thickest anvil regions the CRS only retrieved IWP is smaller than when CoSSIR data is included. The retrieved IWP errors are smaller for CoSSIR only than CRS only retrievals, and decrease further with the

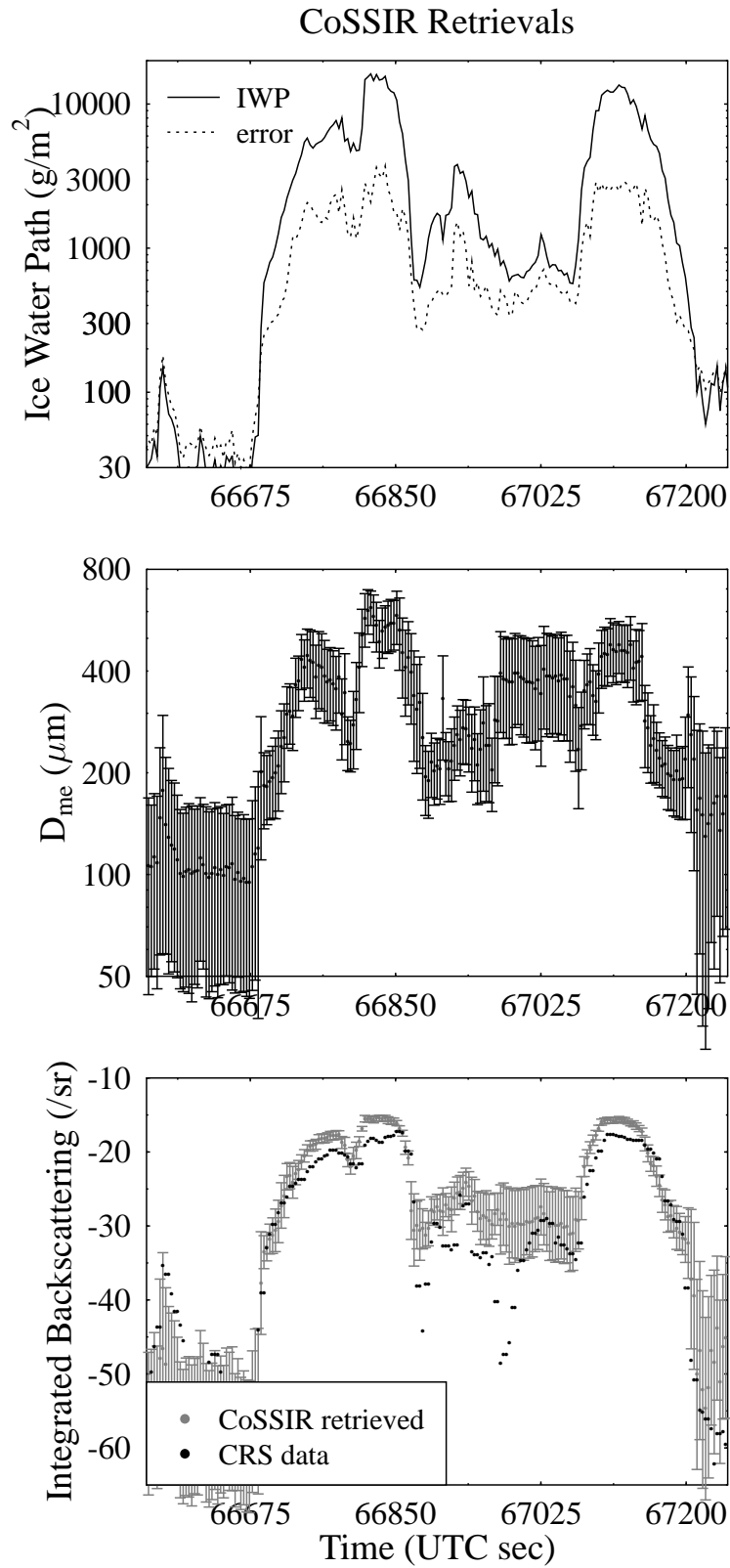


Figure 5: Example retrievals (with  $1\sigma$  errors) of ice water path, median volume equivalent sphere diameter, and vertically integrated backscattering from CoSSIR brightness temperatures on July 3.

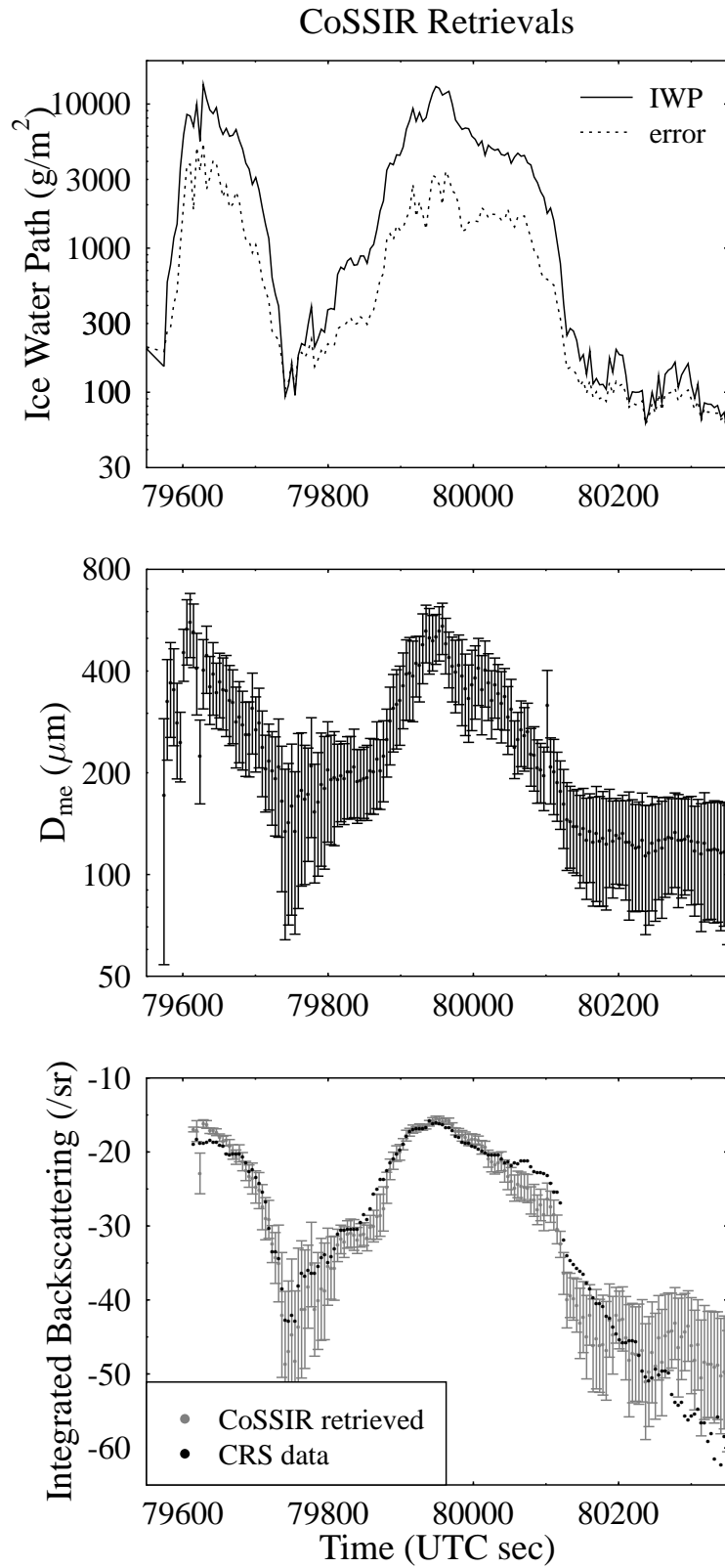


Figure 6: Example retrievals (with  $1 \sigma$  errors) of ice water path,  $D_{me}$ , and integrated backscattering from CoSSIR brightness temperatures on July 28.

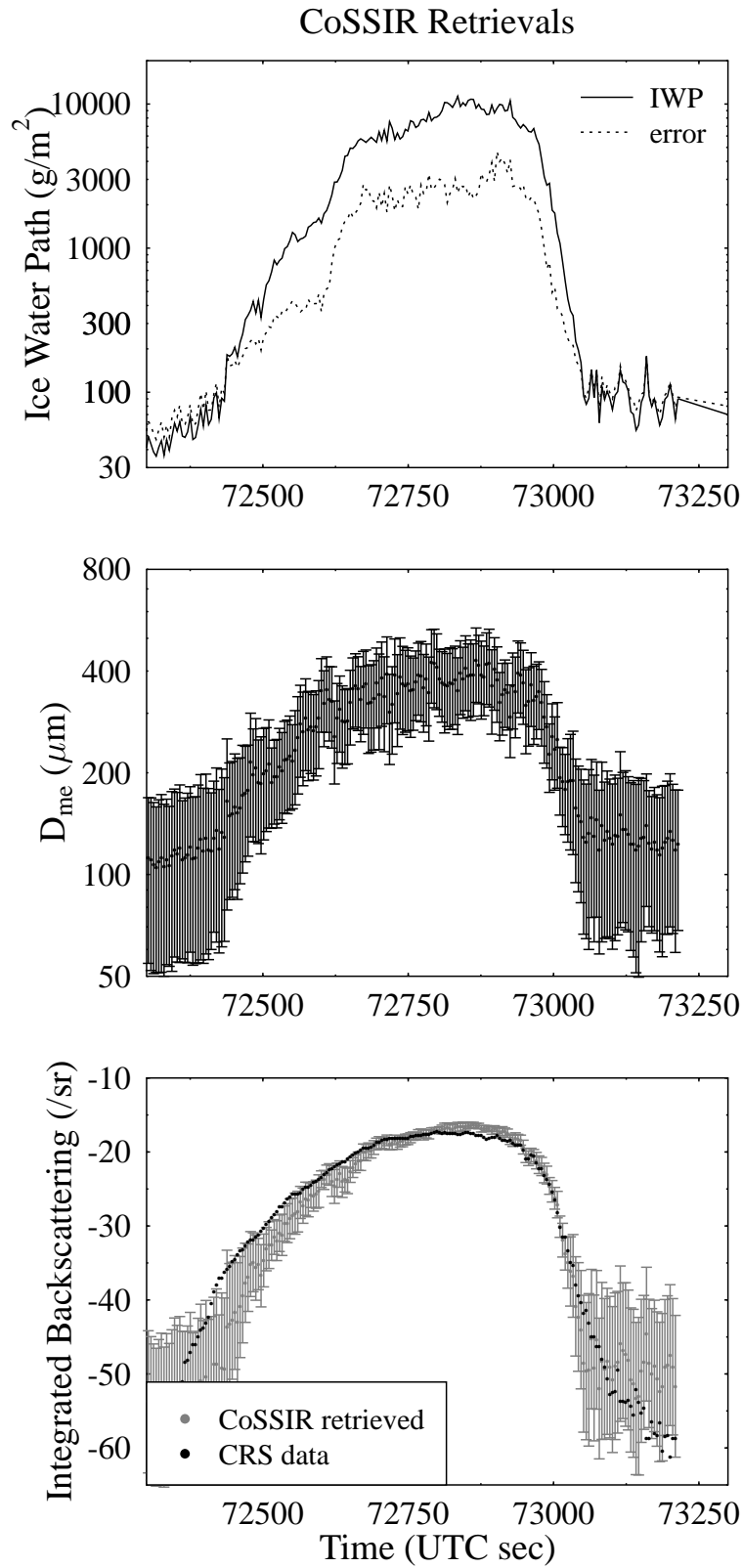


Figure 7: Example retrievals (with  $1 \sigma$  errors) of ice water path,  $D_{me}$ , and integrated backscattering from CoSSIR brightness temperatures on July 29.

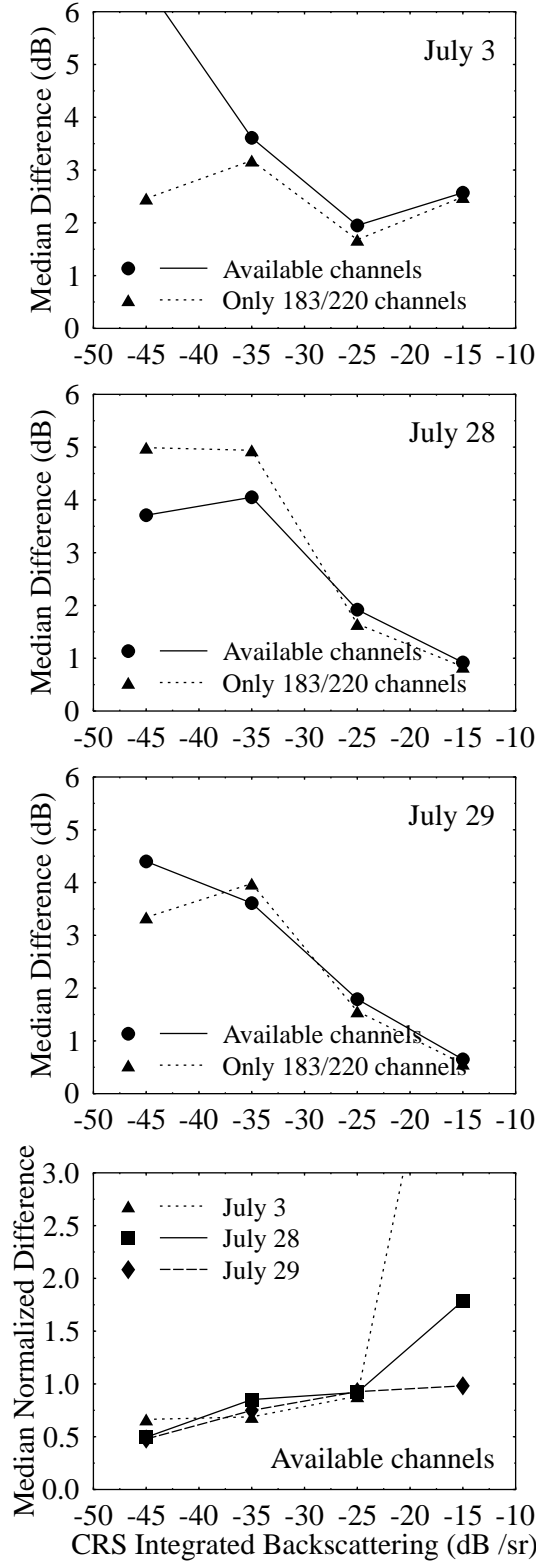


Figure 8: The top three panels show the median absolute difference between CoSSIR retrieved and CRS integrated backscattering as a function of CRS integrated backscattering (in four 10 dB wide bins). The bottom panel shows the median absolute normalized difference, where the normalization is by the retrieved integrated backscattering error.

combination. The  $D_{me}$  errors for the lowest integrated backscattering bin are actually larger for CoSSIR only than for CRS only retrievals because CoSSIR with the noisy submillimeter channels lacks any sensitivity there. In the thicker anvil regions the  $D_{me}$  errors are much lower for the combination of CRS and CoSSIR data than for CRS alone.

## 5. CRS and CoSSIR profile retrievals

A new algorithm was devised to retrieve profiles of IWC and  $D_{me}$  from the combination of CRS radar reflectivity profiles and CoSSIR brightness temperatures. The major assumption of the method is that the ice water content profile is related to the reflectivity profile by  $IWC = 10^{0.1p} Z_e^q$ . However, the coefficients  $p$  and  $q$  are retrieved for each column from the combined CRS and CoSSIR data in a Bayesian integration.

The a priori probability distribution of  $p$  and  $q$  is assumed to be a bivariate Gaussian distribution. The parameters of this distribution (mean and standard deviation of  $p$  and  $q$  and the correlation between them) is obtained from a Monte Carlo simulation using the same microphysical statistics used in the vertically integrated Bayesian retrieval. The IWC and  $D_{me}$  in each of six uniform layers from 4.5 to 15.5 km is obtained by random sampling the bivariate normal distribution of  $\ln(IWC)$  and  $\ln(D_{me})$  given the temperature of that layer. A random scattering table (i.e. a particular particle shape and gamma distribution width) containing the  $D_{me}$  is chosen for each layer. The radar reflectivity  $Z_e$  for a layer is calculated from the IWC and  $D_{me}$  using the scattering table. A linear regression of  $10 \log_{10}(IWC)$  against  $10 \log_{10}(Z_e)$  then gives the  $p$  and  $q$  coefficients for that randomly sampled profile. This process is carried out for 100,000 random profiles to obtain the prior pdf of  $p$  and  $q$ . The means of  $p$  and  $q$  are -7.114 and 0.488, the standard deviations of  $p$  and  $q$  are 1.742 and 0.112, and the correlation between  $p$  and  $q$  is 0.472. The assumption of six independent uniform layers is fairly arbitrary, of course; the standard deviations of  $p$  and  $q$  decrease predictably as the number of independent layers is increased.

A profile retrieval is performed with a Monte Carlo integration over the Bayes theorem posterior pdf. First the radar profile is thresholded to remove noisy pixels (using -30 dBZ at 5 km range) and averaged to the desired vertical resolution over the range (0.25 km from 4.5 to 15.5 km here). The CoSSIR data is merged by interpolation to the CRS time if they are within 3 seconds. For each sample point in the Bayesian integration, a random  $p$  and  $q$  from the a priori distribution are chosen. A random Gaussian distributed 1.0 dB rms offset is added to the reflectivity profile (in dBZ) to simulate calibration uncertainty, and the corresponding IWC profile is calculated from the reflectivity profile using the  $p$  and  $q$ . A scattering table (with one particle shape and gamma distribution width) is chosen randomly for the profile. For each level in the profile the scattering table is used to find a  $D_{me}$  corresponding to the IWC and radar reflectivity  $Z_e$ . Along with the microphysical profile, a random temperature and humidity profile is made using the same technique previously described (in section 3.). The fast radiative transfer method (section 3.) is then used to simulate the CoSSIR  $T_b$ 's from the profile, and hence compute the  $\chi^2$  measure of proximity to the observed  $T_b$ 's. The retrieved IWC and  $D_{me}$  profiles and  $p$  and  $q$  are the mean over the random sample points weighted by the likelihood function,  $\exp(-\chi^2/2)$ . The retrieved error bars are the posterior weighted standard deviation over the integration points. The Bayesian integration loops over a maximum number of random samples (10,000 here), but, to save time, quits early if

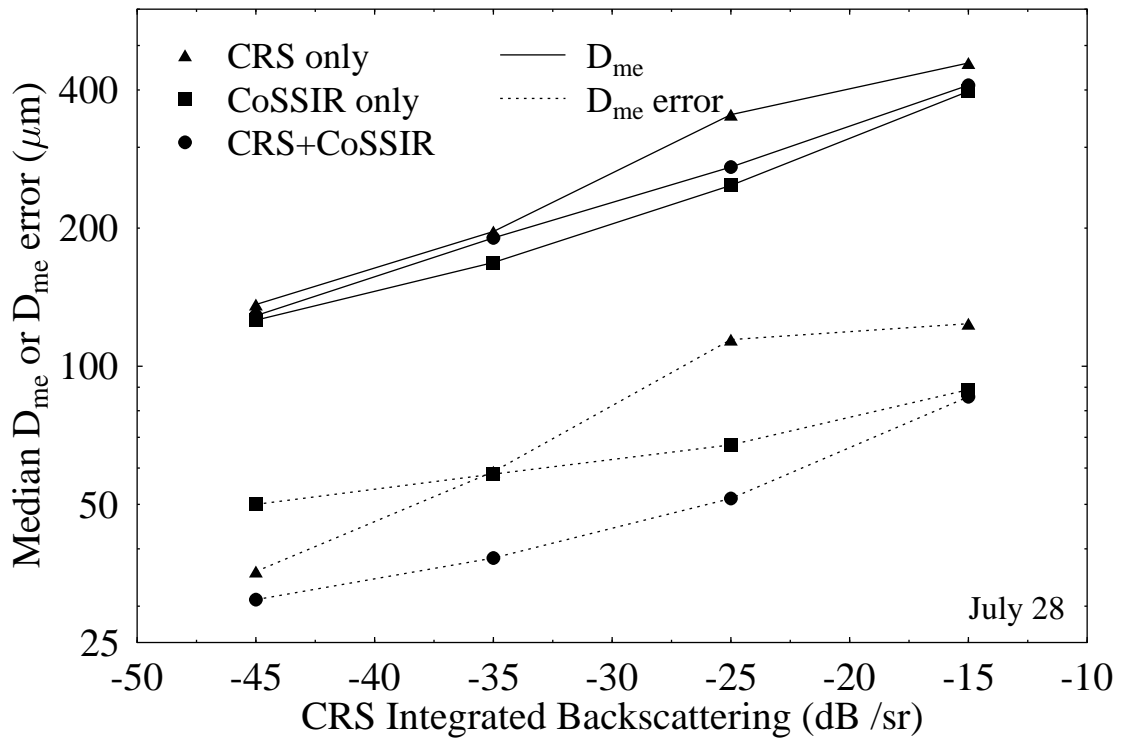
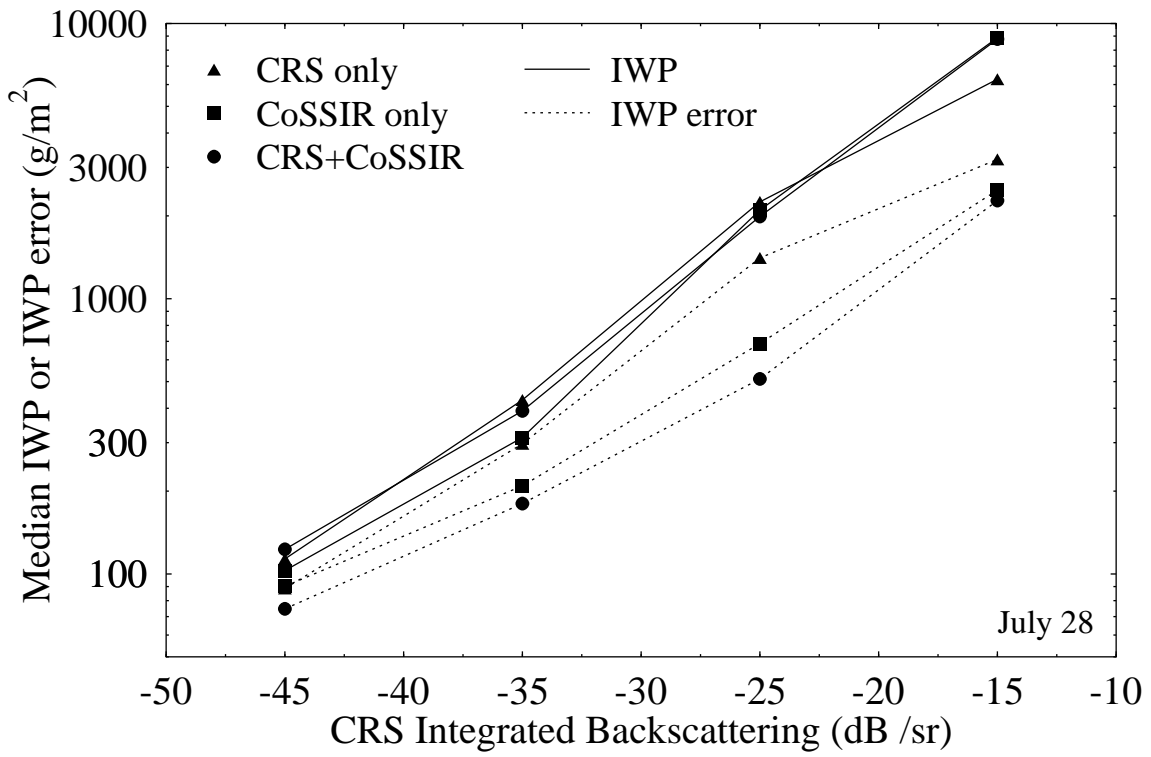


Figure 9: Median retrieved IWP and  $D_{me}$  and errors for three combinations of CRS and CoSSIR data plotted against integrated backscattering (for four 10 dB wide bins).

enough samples with low  $\chi^2$  are obtained (e.g. 400 with  $\chi^2 < M + 3\sqrt{2M}$  for  $M$  CoSSIR channels). The profile retrieving algorithm assumes negligible attenuation of the 94 GHz radar down to 4.5 km. The reflectivity profile is corrected for molecular absorption, but in the thicker anvil regions it also attenuates from particle scattering. An improved algorithm could correct the reflectivity profile by computing the attenuation from a first pass retrieval using the uncorrected profile.

The CRS and CoSSIR profile retrieval algorithm is run for all valid radar profiles on July 3, 28, and 29 using the same CoSSIR channels and  $\sigma$ 's as in section 4.. The same 15 ice particle scattering tables described in appendix B are used. Figure 10 shows an example of the retrieved IWC and  $D_{me}$  profiles. The minor striping seen in the images is due to the relatively small number of points in the Bayesian integration. The retrieved IWC and  $D_{me}$  are not completely correlated as with a standard IWC- $Z_e$  relation, as illustrated by the largest  $D_{me}$  being on the left side of the anvil while the highest IWC is on the right side.

In addition to the profiles, the algorithm also retrieves the coefficients of the IWC- $Z_e$  relation ( $p$  and  $q$ ) and their errors. Figure 11 plots the median  $p$  and  $q$  and errors as a function of the CRS integrated backscattering. The mean and standard deviation of the retrieved coefficients is nearly the same as the prior distribution when the integrated backscattering is below -30 dB. Presumably this is due to the CoSSIR sensitivity being too low to affect the retrievals, which are effectively only from the CRS in the thin anvil regions. At higher integrated backscattering values both the  $p$  and  $q$  coefficients increase away from the prior distribution mean and their uncertainty decreases. In the highest integrated backscattering bin, for example, the median coefficients are  $p = -5.82$  and  $q = 0.566$ , which give a 60% higher IWC for  $Z_e = 10 \text{ mm}^6/\text{m}^3$  than the a priori values (0.96 vs. 0.60  $\text{g}/\text{m}^3$ ).

## 6. Conclusions

The Compact Scanning Submillimeter Imaging Radiometer (CoSSIR) first flew in July 2002 during CRYSTAL-FACE. Scanning across track, CoSSIR measured brightness temperatures in 12 channels with receivers at 183, 220, 380, 487, and 640 GHz. Although the submillimeter-wave channels were noisier than anticipated, the CoSSIR data demonstrate the high sensitivity of the submillimeter channels to ice cloud particles as compared with the lower frequencies. A Bayesian algorithm is used to retrieve ice water path (IWP) and median volume equivalent sphere diameter ( $D_{me}$ ) from the available CoSSIR nadir brightness temperatures. Prior information used by the algorithm is obtained from radiosondes and in situ cloud microphysical probes on the Citation aircraft flown in CRYSTAL-FACE. The retrievals are tested by retrieving vertically integrated 94 GHz radar backscattering from the CoSSIR data, which is then compared to Cloud Radar System (CRS) data. The integrated backscattering typically agrees to 1–2 dB for IWP from 1000 to 10,000  $\text{g}/\text{m}^2$ , while for lower IWP the typical agreement is 3–5 dB, which is within the Bayesian error bars. Retrievals of integrated backscattering using only the 183 and 220 GHz CoSSIR channels have almost as good agreement due to the high noise on the submillimeter channels.

An algorithm was developed to retrieve profiles of ice water content (IWC) and  $D_{me}$  from the combination of CRS reflectivity profiles and CoSSIR brightness temperatures. A power law relation ( $\text{IWC} = 10^{0.1p} Z_e^q$ ) is assumed between IWC and equivalent radar reflectivity ( $Z_e$ ), but the  $p$  and  $q$  coefficients are retrieved for each column. The IWC and  $D_{me}$  profiles

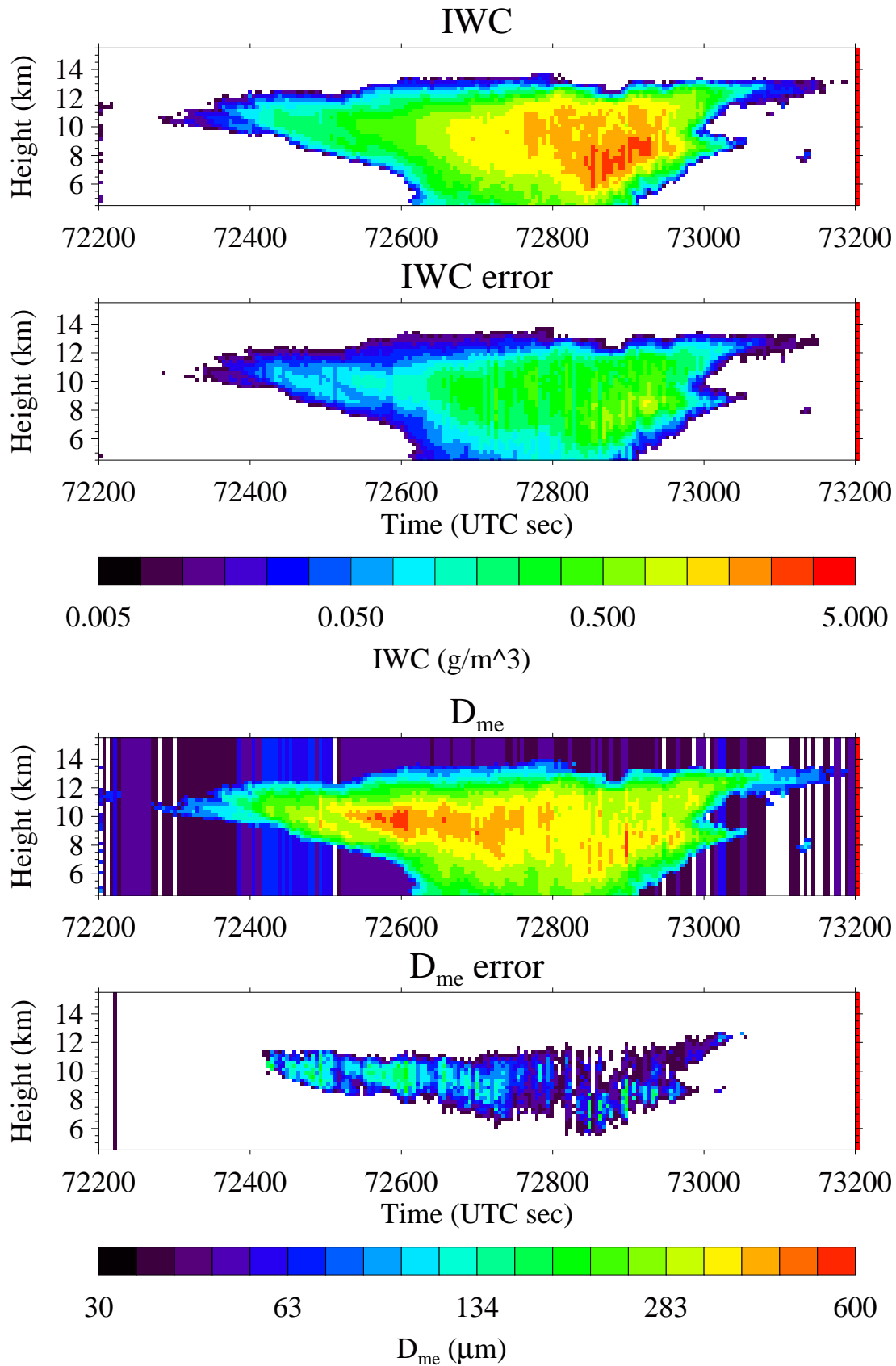


Figure 10: Example IWC and  $D_{me}$  fields from the Bayesian CRS and CoSSIR profile retrieval algorithm for July 29.

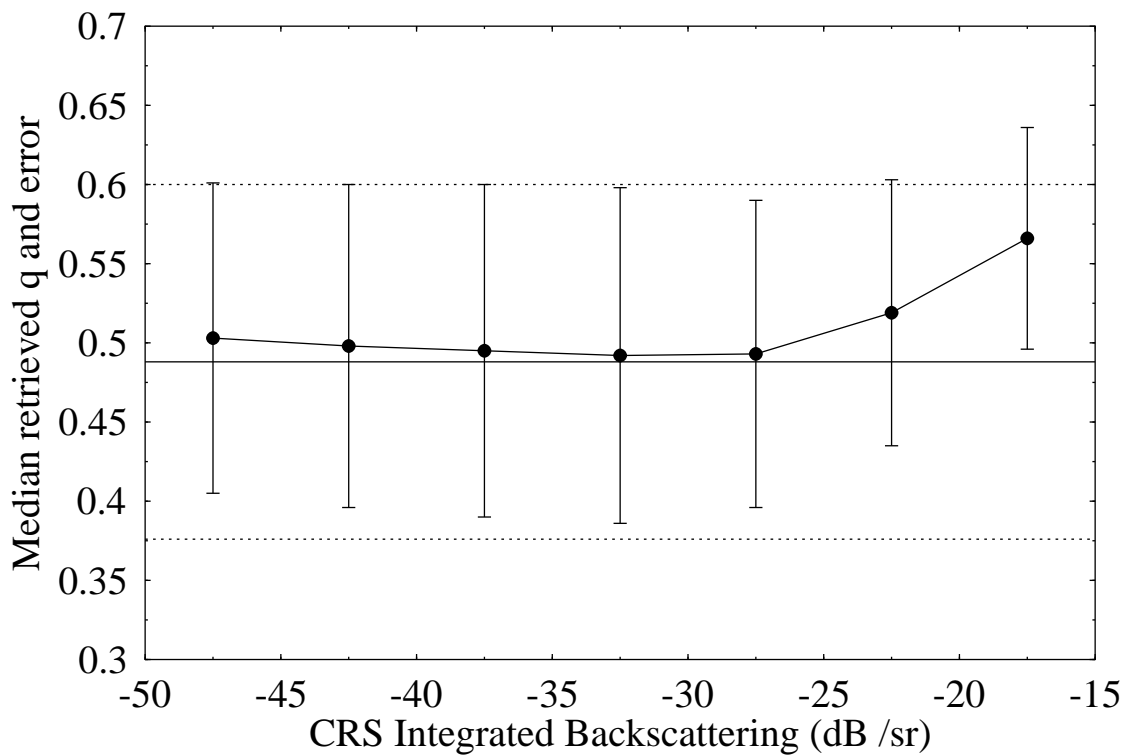
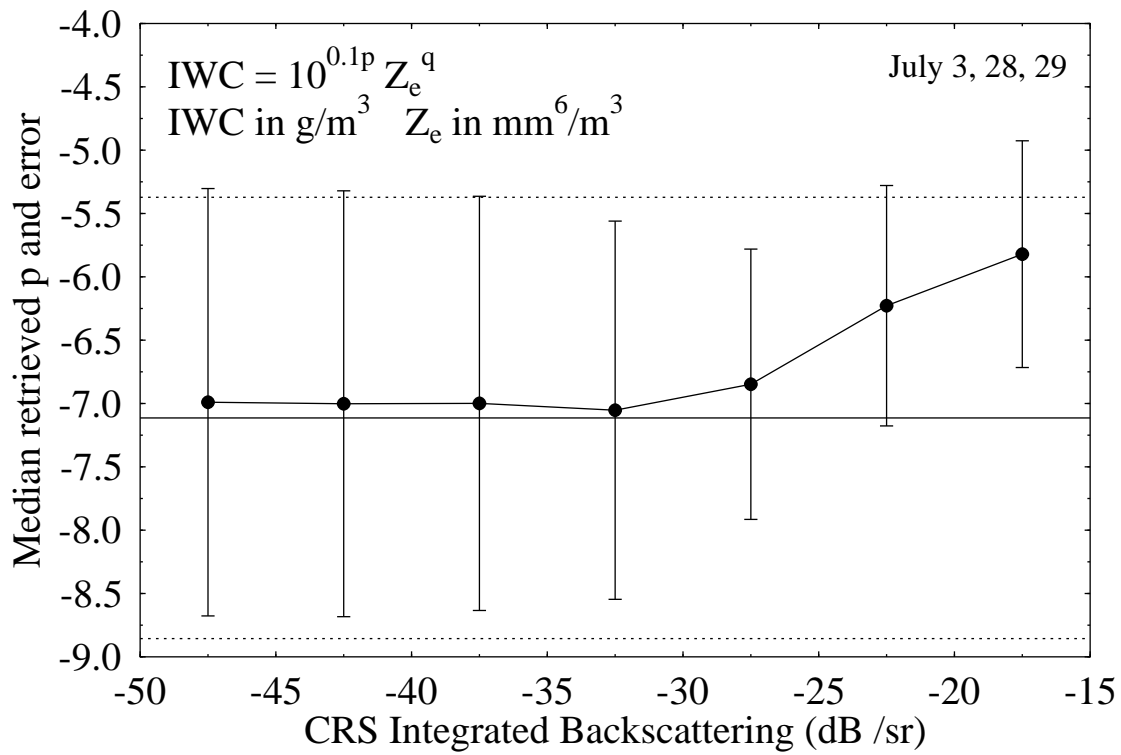


Figure 11: Median retrieved  $p$  and  $q$  and median errors over all flights for the CRS + CoSSIR profile retrieval algorithm. The  $p$  and  $q$  are coefficients in the power law ice water content - radar reflectivity relationship. The solid horizontal lines show the a priori mean values of  $p$  and  $q$ , while the dotted lines show  $\pm$  one standard deviation.

and  $p$  and  $q$  are retrieved in a Bayesian integration that effectively matches the simulated and observed CoSSIR brightness temperatures. The radiometer data adds additional information to the radar profile so that the retrieved IWC and  $D_{me}$  are no longer completely dependent as they are with a traditional IWC- $Z_e$  relation. The median retrieved  $p$  and  $q$  over all flights both increase from the a priori values for the highest IWP clouds. The results from the combined radar-radiometer profile algorithm illustrate how the coefficients for radar only ice cloud retrieval methods could be tuned for particular cloud types using submillimeter radiometer data.

The CoSSIR only retrievals of IWP and  $D_{me}$  and the combined CoSSIR and CRS retrievals of profiles of IWC and  $D_{me}$  are available in the CRYSTAL-FACE archive at <http://espoarchive.nasa.gov/>. During CRYSTAL-FACE the sensitivity of CoSSIR to lower IWP clouds was much poorer than anticipated due to the high noise of the submillimeter-wave channels. CoSSIR is currently being upgraded to improve the performance of the 380, 487, and 640 GHz receivers to noise equivalent temperatures of better than 1.0 K. The CoSSIR upgrade will also include the addition of a 874 GHz receiver for improved sensitivity to cirrus with smaller ice particle size.

**Acknowledgement** The authors wish to thank Andy Heymsfield for microphysical advice and sharing a prepublication manuscript. Andy Heymsfield and Carl Schmitt provided the 2D-C/HVPS size distributions and CPI imagery. Mike Poellot provided the Citation meteorological data and FSSP size distributions, Cyndi Twohy the CVI data, and Larry Miloshevich the radiosonde data, all from the CRYSTAL-FACE archive. KFE was supported in this work by NASA grant NAG5-11501; JRW and PER were supported by NASA grant ??; GH and LL supported by NASA grant ?. The development of CoSSIR was also funded by ?? and ??.

## A Particle size distribution analysis

The Bayesian ice cloud retrieval algorithm requires statistics on the relationship between temperature, IWC, and  $D_{me}$ . For CRYSTAL-FACE the best source of these microphysical statistics are the optical cloud probes on the University of North Dakota Citation aircraft. The Citation flew at a range of lower altitudes compared to the WB-57 aircraft and thus is more representative of the microphysics relevant for vertically integrated retrievals. Cloud probes that measure the particle size distribution are needed to calculate the  $D_{me}$  for each sample. To cover the full range of ice particle sizes, data from three probes are used: the PMS forward scattering spectrometer probe (FSSP), the PMS 2D-C imaging probe, and the SPEC, Inc. high volume particle spectrometer (HVPS). The 2D-C probe has 33  $\mu\text{m}$  resolution, sizes up to 1000  $\mu\text{m}$ , and samples about 0.007  $\text{m}^3/\text{s}$ . The HVPS probe has 200  $\mu\text{m}$  resolution, sizes up to 6000  $\mu\text{m}$ , and samples about 1  $\text{m}^3/\text{s}$ . The FSSP measures size distributions from about 4 to 62  $\mu\text{m}$  and is the only source available for the smaller ice crystals, though the concentrations tend to be overestimates due to large particle breakup and the assumption of particle sphericity.

The composite 2D-C/HVPS size distributions and the FSSP size distributions available from the CRYSTAL-FACE data archive are analyzed in a technique similar to that in Heymsfield et al. (2004). A particle mass - maximum diameter relation of the form  $m = g_0 D^{g_1}$  is assumed, and the coefficients  $g_0$  and  $g_1$  are adjusted to match the IWC measured by the counterflow virtual impactor (CVI) (Twohy et al., 1997). The first step is to average and merge the archived temperature, CVI IWC, and FSSP data to the 5 second samples of the 2D-C/HVPS size distributions for all CRYSTAL-FACE Citation flights. The particle mass for each bin in a measured size distribution may be obtained from the central maximum diameter using the mass-diameter relation for a given  $g_0$  and  $g_1$ . The IWC is then simply the sum over the bins of the particle mass times the number concentration. The procedure for determining the best fitting coefficients has two steps. The first is to try a fixed  $g_1$  and adjust  $g_0$  so that the median (over all samples) of the ratio  $R$  of the computed IWC to the CVI IWC is unity. The coefficient  $g_1$  is then determined by adjusting it to minimize the ratio  $R_{75}/R_{25}$ , where  $R_{25}$  and  $R_{75}$  are the 25th and 75th percentiles, respectively, of the ratio  $R$ . The first step assures an unbiased fit, while the second step minimizes the dispersion of the optical probe IWC around the CVI IWC. We expect that using percentiles is more robust to errors such as the CVI hysteresis. This procedure is carried out only for samples above the nominal CVI sensitivity of 0.01  $\text{g}/\text{m}^3$  and for temperatures below -5 C. The best fitting mass-diameter coefficients from this procedure are  $g_0=0.00423$  and  $g_1=2.12$  in cgs units. Figure 12 shows a scatterplot of the resulting optical probe and CVI IWC. These coefficients give a somewhat lower IWC than those in Heymsfield et al. (2004), which are  $g_0=0.00513$  and  $g_1=2.10$ .

The mass-diameter relation with the tuned coefficients is used to calculate moments of the mass equivalent sphere diameter,  $D_e$ , from the FSSP plus the 2D-C/HVPS size distributions (only samples with nonzero 2D-C/HVPS IWC are used). The IWC and  $D_{me}$  are derived by fitting gamma distributions ( $N(D_e) \propto D_e^\alpha \exp[-(\alpha + 3.67)D_e/D_{me}]$  with  $\alpha = 1$ ) to the third and fourth moments of  $D_e$  (see, e.g. Evans et al., 1998). Processing all 14 Citation flights results in temperature, IWC, and  $D_{me}$  for 13891 samples with IWC above 0.001  $\text{g}/\text{m}^3$ . The microphysical probability distribution in the Bayesian retrieval algorithm

### IWC from 2DC+HVPS+FSSP probes and CVI

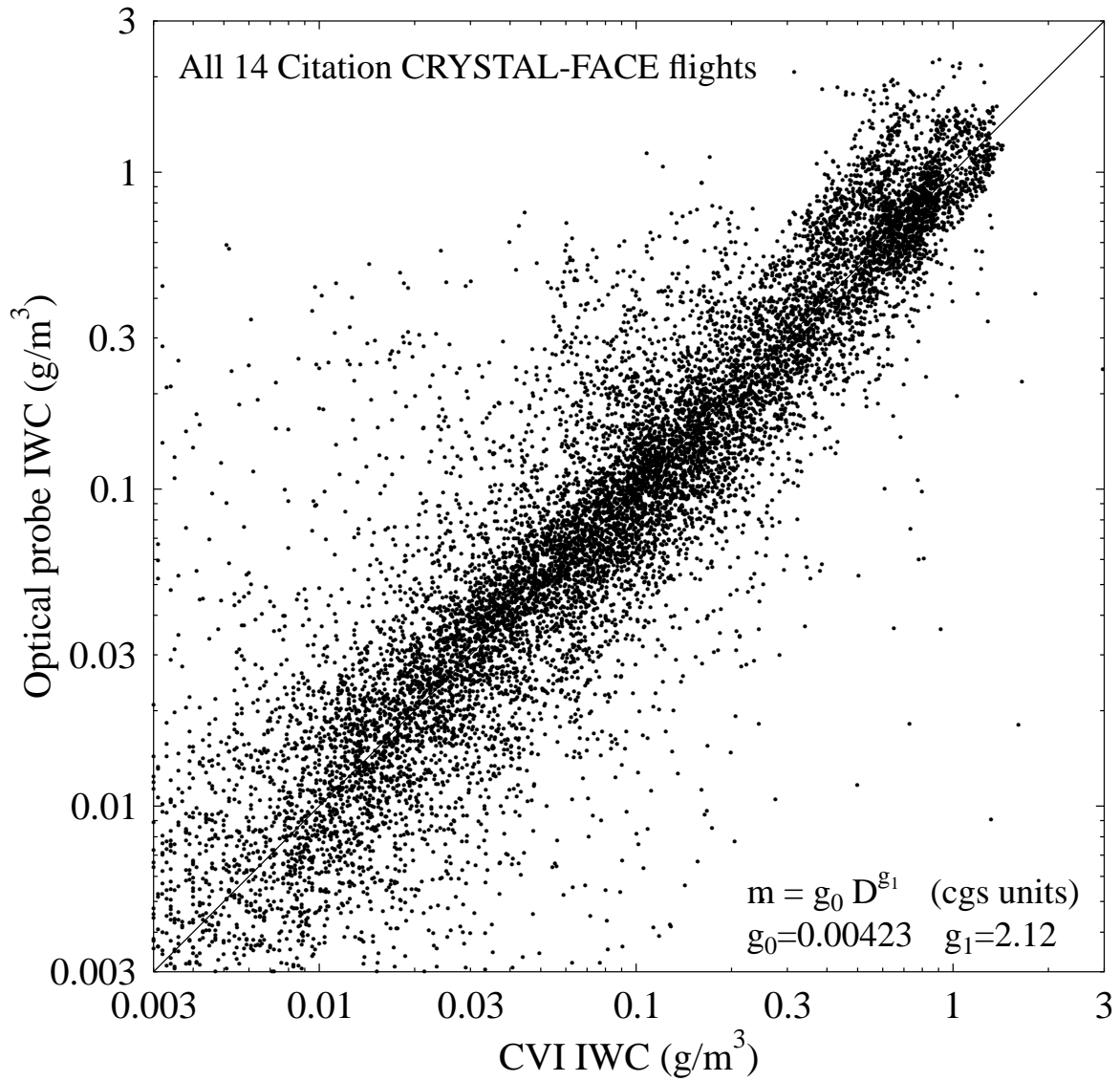


Figure 12: Comparison of the IWC calculated from the optical probe size distributions using the best fitting mass-diameter relation with the counterflow virtual impactor (CVI) IWC.

assumes a Gaussian distribution of temperature. Since the Citation sampling of temperature is experiment dependent and has nothing to do with microphysics, the microphysical samples are randomly selected to make the temperature distribution more Gaussian. This process outputs 5000 samples approximately matching a target distribution with a mean of 235 K and standard deviation of 15 K. Figure 13 shows the relationships between temperature, IWC, and  $D_{me}$  for these 5000 samples. Table 4 lists the statistics of temperature,  $\ln(\text{IWC})$ , and  $\ln(D_{me})$  which are input to the Bayesian retrieval algorithm.

## B Particle shape modeling

The ice particle shapes observed during CRYSTAL-FACE were most often complex irregular particles. Figure 14 shows a typical cloud particle imager (CPI) picture of the particles in a dense part of an anvil. The complex particles often appear to be aggregates of hexagonal plates. In addition there are small, quasi-spherical particles which appear to be frozen droplets. The CoSSIR and CRS retrieval algorithms require us to model the millimeter-wave and submillimeter-wave scattering properties of distributions of these complex particles. The highest CoSSIR frequency is sensitive to features down to about  $50 \mu\text{m}$ , so it is the larger scale particle structure about which we need to be concerned.

The CPI images inspired us to model the complex “junk ice” particles as random aggregates of hexagonal plates and columns. The algorithm for generating these particles starts with a specified number of randomly oriented hexagonal plate and column monomers of a fixed size. An aggregate particle is represented by the position and orientations of the monomers of which it is made. The particles are projected onto Z-buffer images for 46 orientations covering all viewing directions at a spacing of about  $30^\circ$ . A Z-buffer gives the depth (positive or negative) of the particle at each pixel when viewed from a particular direction. Two particles are chosen at random to aggregate, and one of the 46 orientations is also chosen at random for each particle. The two particle Z-buffers for these orientations and a random sideways offset between the two particles are used to determine when the particles touch (a certain amount of overlap may be specified). The two particles are then combined by rotating the first particle to the second particle’s coordinates to make a new aggregate particle. The Z-buffer images are made for the new aggregated particle. This process of aggregating (potentially already aggregated) particles proceeds until there is only one particle left, which contains all of the original monomers.

Three sets of random hexagonal aggregate particles are created. The first set of 20 sizes of hexagonal plate aggregates has monomers with a maximum diameter of  $230 \mu\text{m}$  and thickness of  $25 \mu\text{m}$ . The second set of 20 sizes of plate aggregates has thicker plates with a maximum

Table 4: Microphysical Input Statistics

	Temperature (K)	$\ln(\text{IWC}[\text{g}/\text{m}^2])$	$\ln(D_{me}[\mu\text{m}])$
mean	236.5	-2.65	5.09
std. dev.	12.2	1.82	0.766
correlation	$\rho_{T-IWC} = 0.402$	$\rho_{T-D_{me}} = 0.605$	$\rho_{IWC-D_{me}} = 0.586$

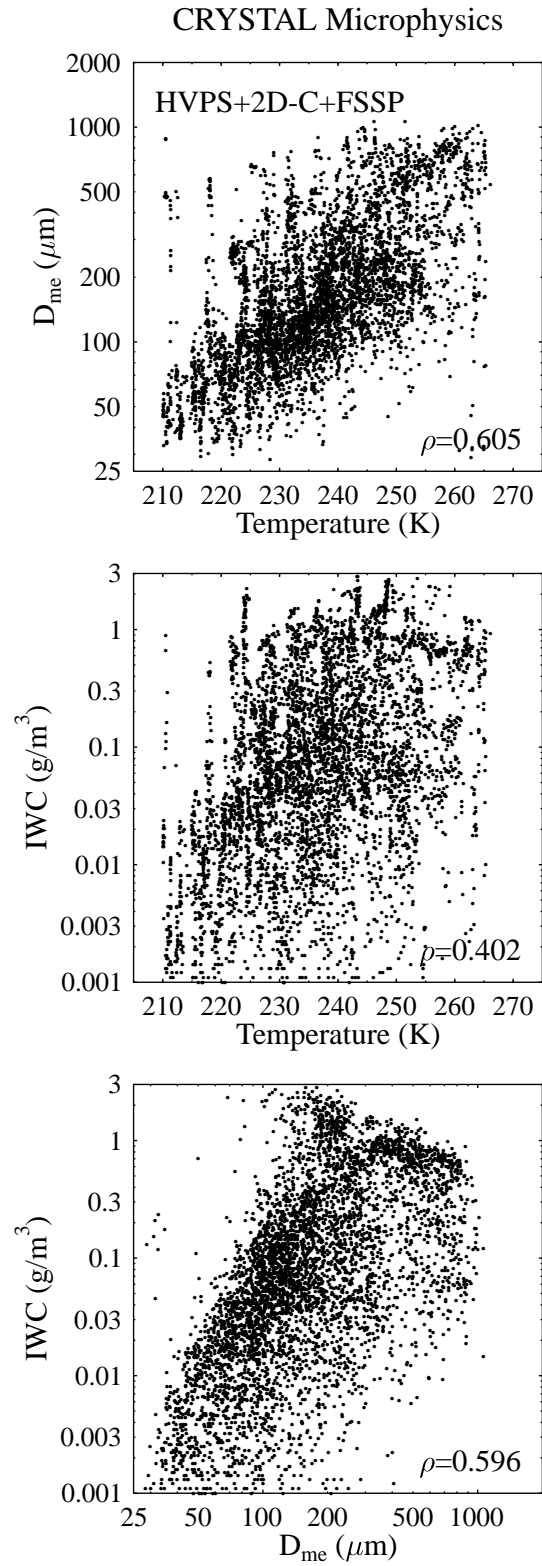


Figure 13: Comparison of the IWC calculated from the optical probe size distributions using the best fitting mass-diameter relation with the counterflow virtual impactor (CVI) IWC.

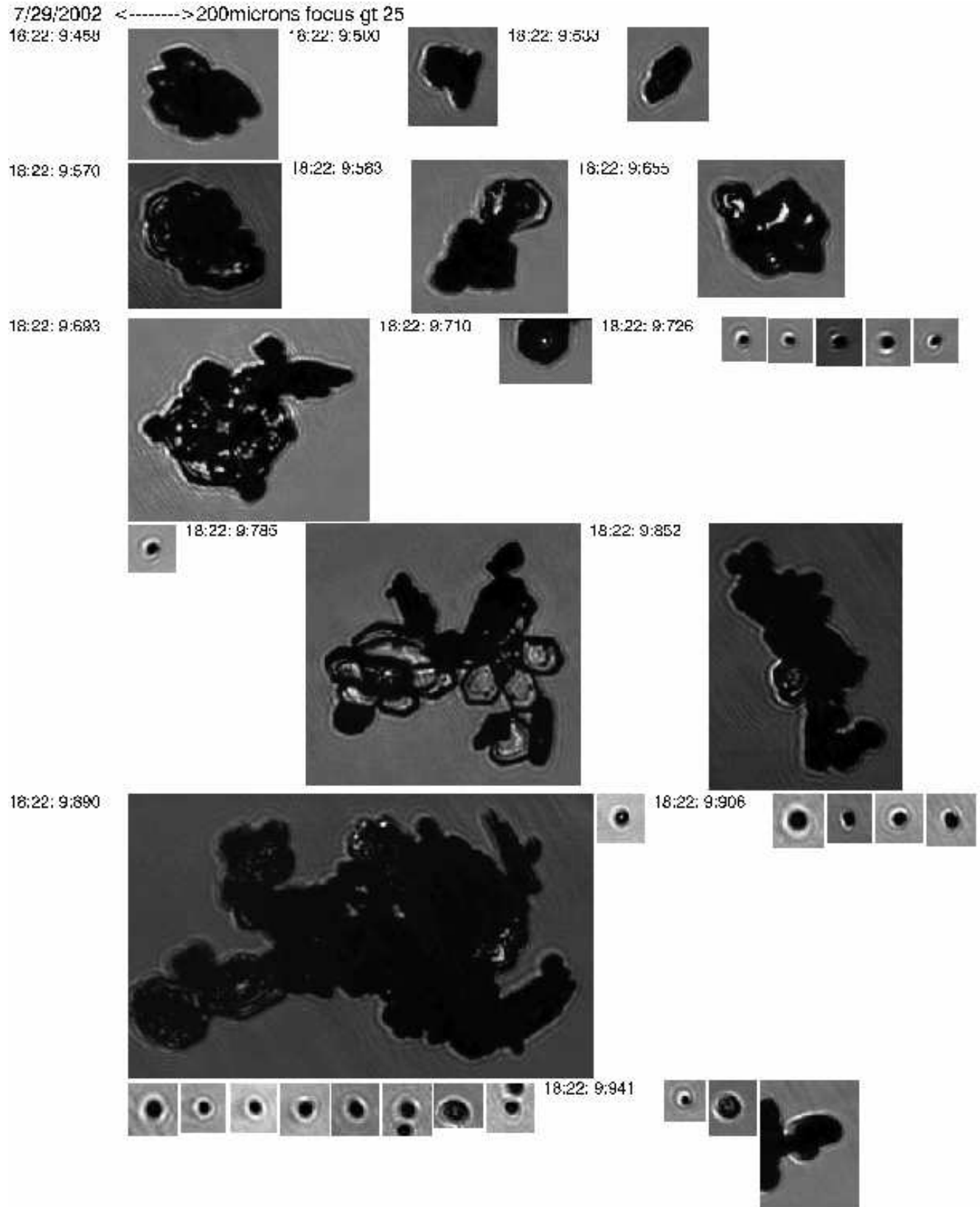


Figure 14: A Citation cloud particle imager display showing ice particle shapes from a thick anvil region at 18:22:10 UTC on July 29.

diameter of  $210 \mu\text{m}$  and thickness of  $30 \mu\text{m}$ . The last set has plates (diameter of  $230 \mu\text{m}$  and thickness of  $25 \mu\text{m}$ ) for 75% of the monomers and hexagonal columns (diameter of  $115 \mu\text{m}$  and length of  $300 \mu\text{m}$ ) for 25% of the monomers (18 particle sizes). Figure 15 shows one example particle image from each of the three sets. The maximum number of monomers modeled is determined by the computational limits of the light scattering code. Table 5 lists the orientation average maximum diameter, equivalent volume sphere diameter, and equivalent area sphere diameter for the smallest (a single monomer) and largest aggregate of each type. In spite of the computational limit, the average maximum diameter ranges up to 1.5 to 1.8 mm depending on the type of aggregate. The plate/column aggregates are supplemented with 7 solid ice spheres with diameters from 20 to  $80 \mu\text{m}$  to simulate the quasi-spherical particles seen in the CPI images.

CPI images from the WB-57, which flew at higher altitudes than the Citation, show chains of quasi-spherical particles, perhaps aggregated by the electric fields in the anvil tops. The more convective parts of these cloud systems are likely to have graupel particles. Both of these particle types can be modeled by random aggregates of small ice spheres. The random sphere aggregation algorithm is similar to the hexagonal plate and column aggregation method, but simpler. The spheres are sent into the particle one at a time, so that there is no aggregation of aggregates. In this use each sphere monomer is sent into a random orientation of the particle (however, a fixed orientation gives a nice conical shaped graupel particle). Two sets of random sphere aggregates are made with two sizes of monomer spheres ( $30$  and  $40 \mu\text{m}$ ). Over the 23 sizes of sphere aggregates the number of monomers ranges up to 3600, the average maximum diameter goes up to 1.00 mm or 1.32 mm (for  $30$  or  $40 \mu\text{m}$  spheres), and the equivalent volume diameter ranges up to 0.460 mm or 0.613 mm. Figure 16 shows two of the sphere aggregate particles.

The single scattering information for the randomly oriented particles described above is computed with the Discrete Dipole Approximation (DDA) at the frequencies of CoSSIR and

Table 5: Diameter statistics for the random hexagonal aggregate particles.<sup>1</sup>

Shape	$N_{mono}$	$\langle D_{max} \rangle$ (mm)	$D_{eqvol}$ (mm)	$D_{eqarea}$ (mm)
plate1	1	0.183	0.118	0.165
plate1	40	1.566	0.451	1.017
plate2	1	0.162	0.118	0.155
plate2	76	1.858	0.553	1.222
plate-column	40	1.493	0.462	0.913

<sup>1</sup>  $N_{mono}$  is the number of monomers from which the aggregate is made.  $\langle D_{max} \rangle$  is the average maximum particle extent over 46 orientations.  $D_{eqvol}$  is the volume equivalent sphere diameter, and  $D_{eqarea}$  is the area equivalent sphere diameter. The shape plate1 refers to the thinner plate aggregates, plate2 to the thicker plate aggregates, and plate-column to the aggregates of 75% plates and 25% columns.

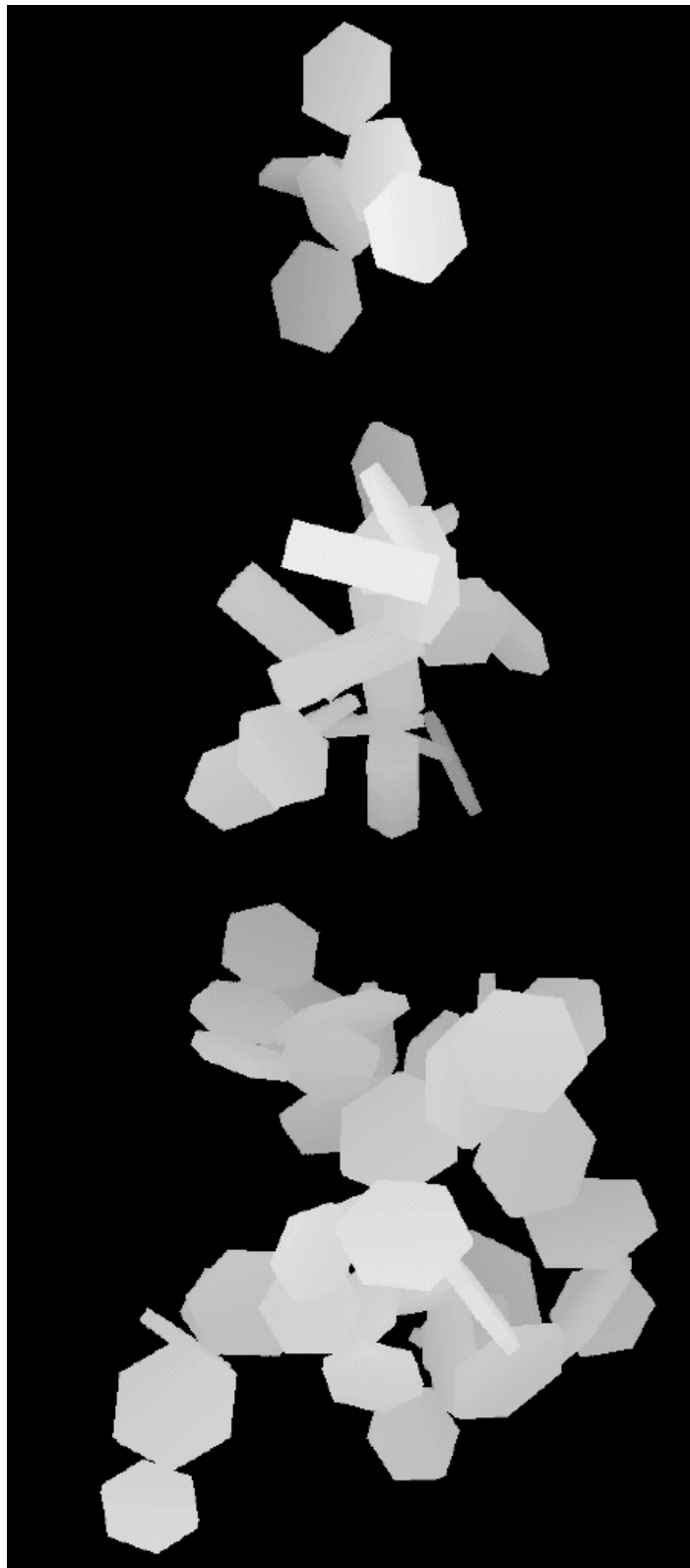


Figure 15: Z-buffer images showing one particle from each of the three sets of random hexagonal aggregates. The top image shows an aggregate of 6 of the thinner plates, the middle image shows an aggregate of 20 plates and columns, and the bottom image shows an aggregate of 40 thicker plates. The lighter shades indicate the closer parts of the particle, and the darker shades indicate the farther parts.

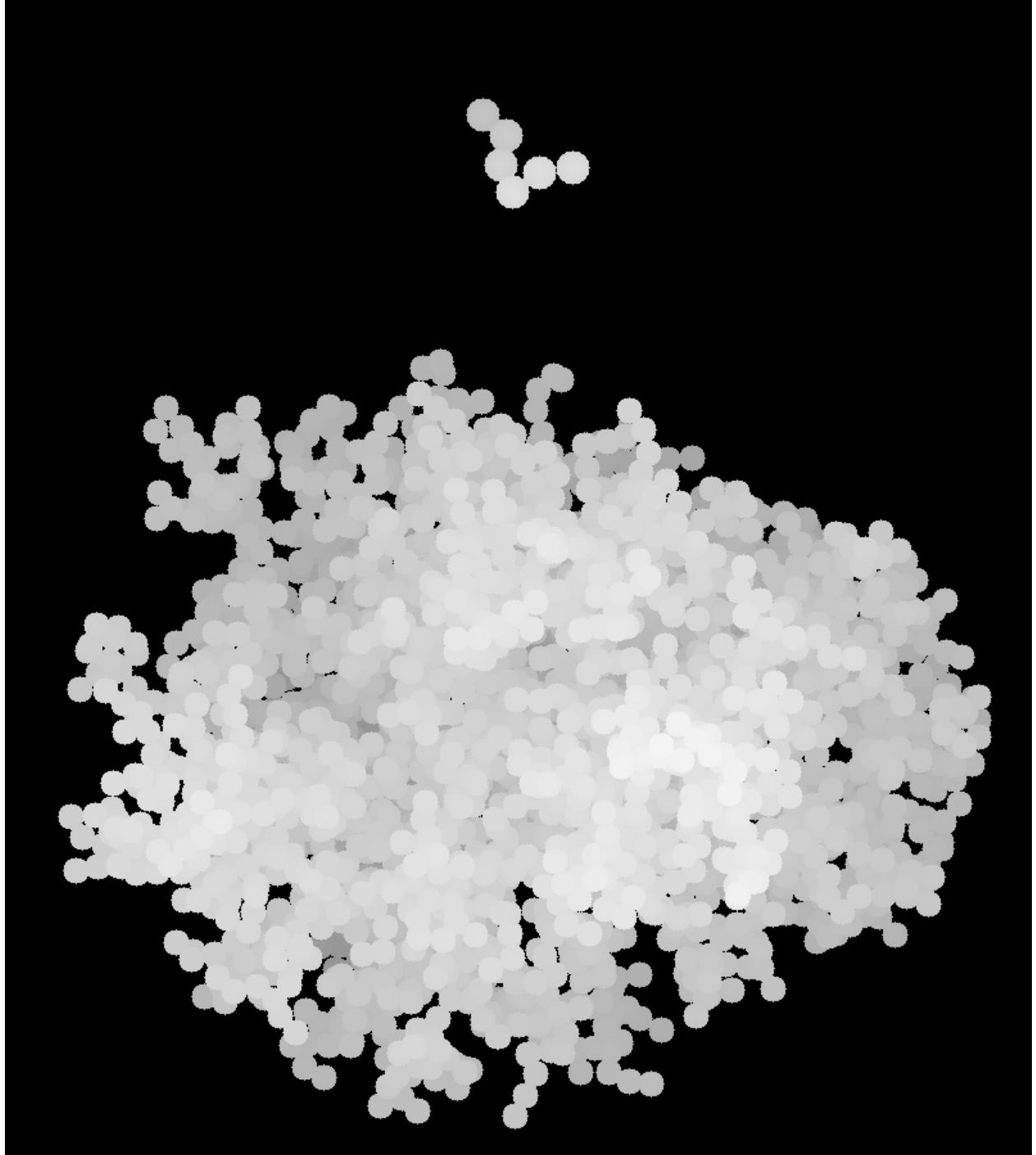


Figure 16: Z-buffer images showing two random sphere aggregate particles. The top image shows an aggregate of 6 spheres ( $40 \mu\text{m}$  diameter), and the bottom image shows an aggregate of 3600 spheres ( $30 \mu\text{m}$  diameter).

CRS (see Evans and Stephens (1995a) for a description of the DDA code). A particle is divided into a number of dipoles: for the sphere aggregates each sphere monomer is a dipole, while for the hexagonal aggregates the dipole size is equal to the plate thickness. The dipoles are arrayed on a lattice oriented along each hexagonal plate or column monomer, and grid cells with more half their volume inside the particle have a dipole assigned (partial volume dipoles with a reduced index of refraction are not used). This method of allocating dipoles at arbitrary positions requires using the DDA matrix inversion method. The inversion method is actually far faster than the FFT-conjugate-gradient solution method, because the latter requires a uniform lattice of dipole sites (hence many more, partially filled dipoles) and the solution method must be repeated for each incident direction. The maximum number of dipoles, however, is limited to 3600 for a computer with 1 GB of memory (due to the  $3N \times 3N$  complex dipole interaction matrix for  $N$  dipoles). The orientation average is performed with incident directions at 16 zenith angles times 32 azimuth angles. Although these random aggregate particles would not be expected to be completely randomly oriented, the fast Eddington radiative transfer model requires random orientation, so that the single scattering properties are defined by the extinction, single scattering albedo, and the asymmetry parameter.

Figure 17 shows the three scattering properties for the lowest and highest CoSSIR frequencies as a function of the equivalent volume sphere diameter,  $D_e$ . There is a significant, but modest, difference in extinction and single scattering albedo between sphere aggregates and hexagonal aggregates for  $D_e$  above about  $150 \mu\text{m}$ . There is a large difference, however, in asymmetry parameter between the particle shapes, which affects the CoSSIR radiances substantially.

Even though the average maximum diameter of the largest sphere aggregate (with 3600 spheres) is above 1 mm, particles with  $D_e$  larger than  $600 \mu\text{m}$  are needed for the deeper, more convective parts of the clouds. Given the computational limits of the DDA method, we chose to calculate the scattering properties of larger sphere aggregates with a tuned effective medium approximation. Effective medium approximations use “mixing rules” to calculate an effective index of refraction for the mixture of ice and air in a heterogenous particle. These theories assume a uniform mixture with ice (or air) inclusions that are very small compared to the wavelength (e.g. Chylek et al., 2000). Since these assumptions are violated for ice particles at submillimeter wavelengths, it is best to use mixing rules in an empirical fashion. Besides the choice of a particular mixing rule, one can also choose the diameter of the sphere to represent the nonspherical particle (and hence the volume fraction of ice to use in the mixing rule). The approach taken here is to try several mixing rules and several definitions of effective diameter and to choose the best combination for matching Mie theory to the DDA scattering results. Then the Mie theory mixing rule method is used to extrapolate the scattering results to larger  $D_e$  for the sphere aggregate particles. The mixing rules tried were Lorentz-Lorenz, Bruggeman, and inverse Maxwell-Garnett (air inclusions in ice). The Lorentz-Lorenz mixing rule is defined by

$$\frac{\epsilon_{eff} - 1}{\epsilon_{eff} + 2} = v \frac{\epsilon_i - 1}{\epsilon_i + 2}, \quad (5)$$

where  $\epsilon_{eff} = m_{eff}^2$  is the effective dielectric constant,  $m_{eff}$  is the effective index of refraction,  $\epsilon_i$  is the dielectric constant of ice, and  $v$  is the ice volume fraction. The effective diameters

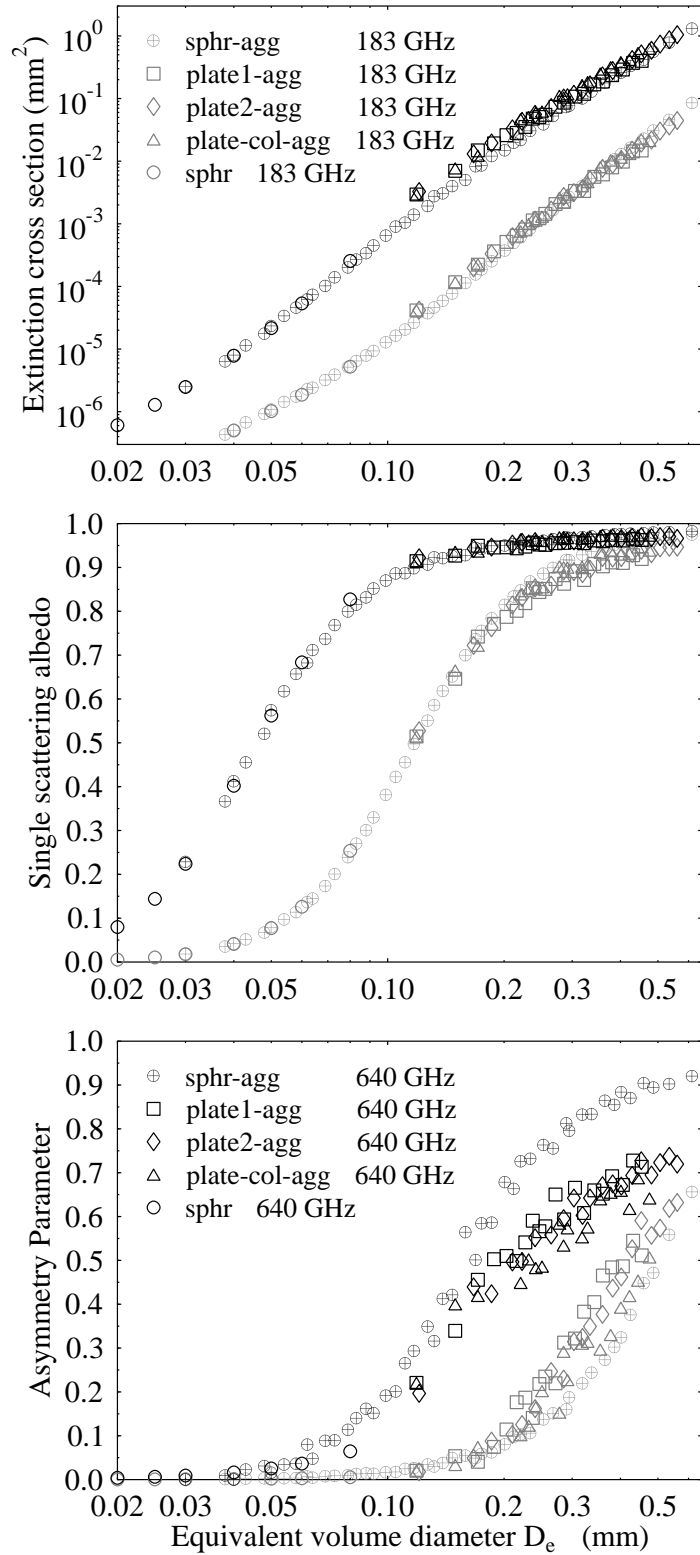


Figure 17: The extinction, single scattering albedo, and asymmetry parameter for the four random aggregate particle shapes at 183 and 640 GHz. The small spheres that supplement the hexagonal aggregates are also shown. The aggregates with  $30 \mu\text{m}$  and  $40 \mu\text{m}$  spheres are combined into one particle type.

tried include the equivalent volume sphere diameter (i.e. an ice volume fraction of unity), the average maximum diameter, the root mean square weighted diameter, the root mean cubed weighted diameter, and the root mean sixth moment weighted diameter. The latter three diameters are defined by

$$D_{rm,n} = 2 \left( \frac{1}{N} \sum_{i=1}^N r_i^n \right)^{1/n} \quad (6)$$

where  $r_i$  is the distance of the sphere monomer from the center of mass,  $N$  is the number of sphere monomers, and  $n$  is 2, 3, or 6.

Figure 18 shows the most relevant results comparing Mie theory with a mixing rule to the DDA scattering results for sphere aggregates. Using Mie theory for solid ice spheres (diameter equal to  $D_e$ ) gives extinction much too high and asymmetry parameter much too low. Using the average maximum diameter (a reasonable way to define the actual diameter of a sphere aggregate) and the Lorentz-Lorenz mixing rule results in the extinction being too low and the asymmetry parameter being too high. The best effective diameter definition is the sixth moment weighted diameter, which gives accurate results especially above  $D_e = 0.3$  mm, where the aggregate is made up of a large number of spheres. The Bruggeman mixing rule results are quite similar to the Lorentz-Lorenz ones, while inverse Maxwell-Garnett does not work well and is also not very physical. The sphere aggregate scattering properties are then extended to larger sizes by making each random aggregate particle (up to 60,000 sphere monomers), calculating the sixth moment diameter  $D_{rm6}$  and the corresponding volume fraction, determining the Lorentz-Lorenz effective index of refraction, and computing the Mie scattering properties.

The Bayesian retrieval database should include different shapes at all particle sizes ( $D_e$ ), so that there is realistic variability in this radiatively important parameter. However, with the particle shapes describe above there are only sphere aggregates for  $D_e > 0.55$  mm. To increase the variability in scattering properties for the larger particle sizes, a fifth particle type is modeled: low density spheres, perhaps representing snow aggregates. The volume fraction of the sphere aggregates at the largest sizes is 0.22 to 0.24 (using the  $D_{rm6}$  diameter), so we choose a volume fraction of 0.1. The Lorentz-Lorenz mixing rule and Mie theory are used to compute the scattering properties of these low density spheres for  $D_e$  from 0.080 mm to 1.60 mm.

For each particle type the computed scattering properties are summed over gamma distributions of the particle sizes. The gamma distributions are defined by  $N(D_e) \propto D_e^\alpha \exp[-(\alpha + 3.67)D_e/D_{me}]$ , where  $D_e$  is the equivalent sphere diameter. To deal with the truncation of the size distribution from the finite range of particle sizes, the  $D_{me}$  and  $\alpha$  for a discrete distribution are adjusted so that the 4th and 6th moments (in addition to the IWC) matches those of a theoretical continuous gamma distribution with the desired  $D_{me}$  and  $\alpha$ . The  $D_{me}$  and  $\alpha$  calculated from the moments must match the desired values within specified tolerances (2% for  $D_{me}$  and 0.5 in  $\alpha$  are used here). This limits the range of allowed  $D_{me}$  in a scattering table made for a particular particle type and  $\alpha$ . As shown in Table 6 the narrowest distribution  $\alpha = 7$  has the largest range of  $D_{me}$ . The available  $D_{me}$  in the scattering tables affects the distribution of clouds in the retrieval database because randomly selected clouds that have a  $D_{me}$  at cloud top or base outside the allowed range for the randomly chosen scattering table are rejected.

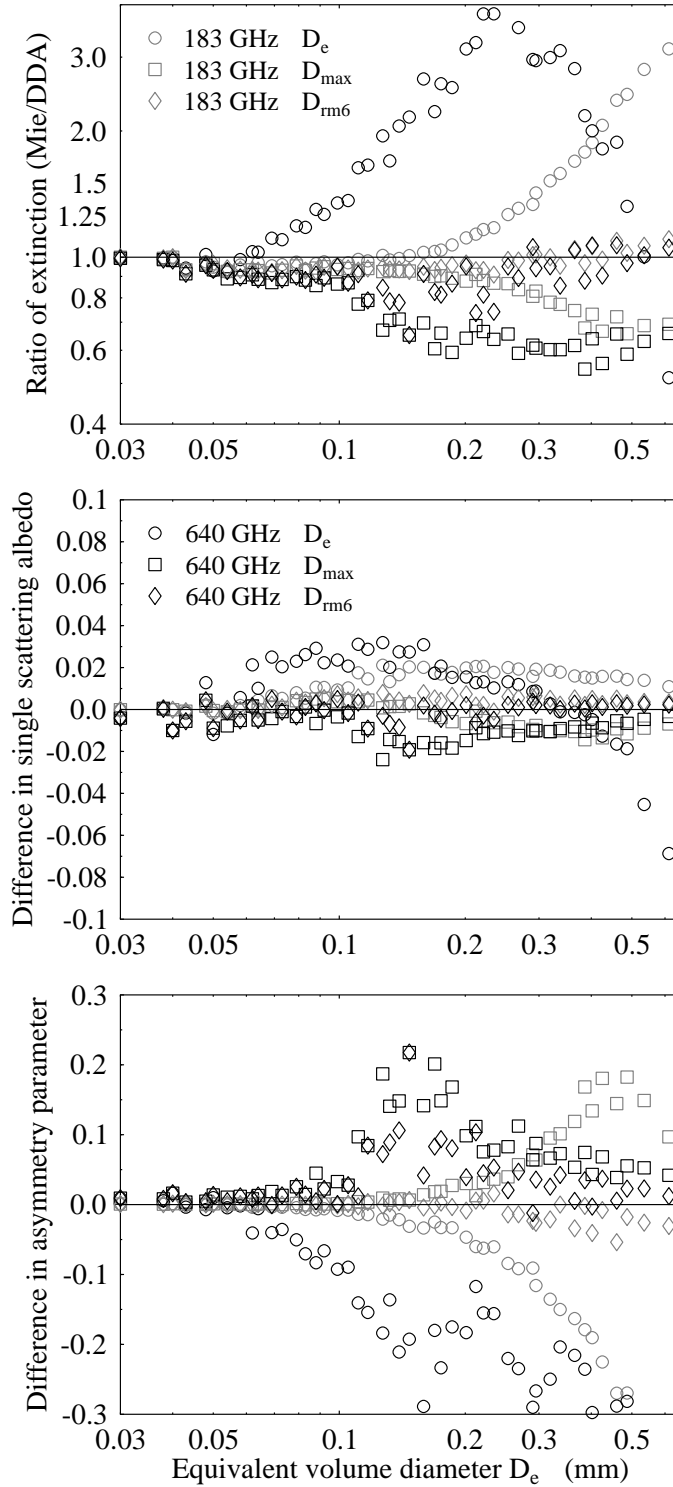


Figure 18: The errors in extinction, single scattering albedo, and asymmetry parameter from using Mie theory to approximate the scattering properties of random sphere aggregates (computed with DDA). The points labeled  $D_e$  (circles) are for Mie theory with no mixing rule on spheres having the equivalent volume sphere diameter. The points labeled  $D_{max}$  (squares) are for Mie theory with the Lorentz-Lorenz mixing rule on spheres having the the average maximum aggregate diameter. The points labeled  $D_{rm6}$  (diamonds) are for Mie theory with the Lorentz-Lorenz mixing rule on spheres having the sixth power weighted diameter.

Table 6: Range of  $D_{me}$  ( $\mu\text{m}$ ) in scattering tables.<sup>1</sup>

Shape	$\alpha = 0$		$\alpha = 2$		$\alpha = 7$	
	min	max	min	max	min	max
sphr(vf=0.1)	126	800	112	898	100	1270
sphr-agg	50	713	45	898	40	1131
plate1-agg	32	225	28	252	25	318
plate2-agg	32	252	28	318	25	400
plate-col-agg	32	225	28	283	25	318

<sup>1</sup>Minimum and maximum  $D_{me}$  in the 15 scattering tables used in the retrievals. “sphr(vf=0.1)” refers to the low density spheres with volume fraction of 10% ice. The hexagonal plate/column aggregate distributions also include small solid ice spheres (20 to 80  $\mu\text{m}$  diameter). The scattering tables have  $D_{me}$  steps of a factor of  $2^{1/6}$  (about 0.5 dB).

## References

- Chylek, P., G. Videen, D. J. W. Geldart, J. S. Dobbie, and H. C. W. Tso: 2000, Effective medium approximations for heterogeneous particles. *Light Scattering by Nonspherical Particles: Theory, Measurement, and Applications*, M. I. Mishchenko, J. W. Hovenier, and L. D. Travis, eds., Academic Press, chapter 9, 274–308.
- Deeter, M. N. and K. F. Evans: 2000, A novel ice-cloud retrieval algorithm based on the millimeter-wave imaging radiometer (MIR) 150- and 220-GHz channels. *J. Appl. Met.*, **39**, 623–633.
- Durden, S. L., E. Im, F. K. Li, W. Picketts, A. Tanner, and W. Wilson: 1994, ARMAR: An airborne rain-mapping radar. *J. Atmos. Ocean. Tech.*, **12**, 727–737.
- Evans, K. F. and G. L. Stephens: 1995a, Microwave radiative transfer through clouds composed of realistically shaped ice crystals. Part I: Single scattering properties. *J. Atmos. Sci.*, **52**, 2041–2057.
- 1995b, Microwave radiative transfer through clouds composed of realistically shaped ice crystals. Part II: Remote sensing of ice clouds. *J. Atmos. Sci.*, **52**, 2058–2072.
- Evans, K. F., S. J. Walter, A. J. Heymsfield, and M. N. Deeter: 1998, Modeling of submillimeter passive remote sensing of cirrus clouds. *J. Appl. Met.*, **37**, 184–205.
- Evans, K. F., S. J. Walter, A. J. Heymsfield, and G. M. McFarquhar: 2002, The submillimeter-wave cloud ice radiometer: Simulations of retrieval algorithm performance. *J. Geophys. Res.*, **107(D3)**, 10.1029/2001JD000709.

- Gasiewski, A. J.: 1992, Numerical sensitivity analysis of passive EHF and SMMW channels to tropospheric water vapor, clouds, and precipitation. *IEEE Trans. Geosci. Remote Sensing*, **30**, 859–870.
- Heymsfield, A. J., A. Bansemer, C. Schmitt, C. Twohy, and M. R. Poellot: 2004, Effective ice particle densities derived from aircraft data. *J. Atmos. Sci.*, in Press.
- Li, L., G. M. Heymsfield, P. E. Racette, T. Lin, and E. Zenker: 2003, The 94 GHz cloud radar system on a NASA ER-2 aircraft. *J. Atmos. Ocean. Tech.*
- Liu, G. and J. A. Curry: 2000, Determination of ice water path and mass median particle size using multichannel microwave measurements. *J. Appl. Met.*, **39**, 1318–1329.
- Rossow, W. B. and R. A. Schiffer: 1999, Advances in understanding clouds from ISSCP. *Bull. Amer. Meteor. Soc.*, **80**, 2261–2287.
- Sekelsky, S. M. and R. E. McIntosh: 1996, Cloud observations with polarimetric 33 GHz and 95 GHz radar. *Meteor. and Atmos. Phys.*, **59**, 123–140.
- Stephens, G. L., D. G. Vane, R. J. Boain, G. G. Mace, K. Sassen, Z. Wang, A. J. Illingworth, E. J. O’Connor, W. B. Rossow, S. L. Durden, S. D. Miller, R. T. Austin, A. Benedetti, C. Mitrescu, and The CloudSat Science Team: 2002, The CloudSat mission and the A-train: A new dimension of space-based observations of clouds and precipitation. *Bull. Amer. Meteor. Soc.*, **83**, 1771–1790.
- Stubenrauch, C., R. Holz, A. Chedin, D. L. Mitchell, and A. J. Baran: 1999, Retrieval of cirrus ice crystal sizes from 8.3 and 11.1 micron emissivities determined by the improved initialization inversion of TIROS-N Operational Vertical Sounder observations. *J. Geophys. Res.*, **104**, 793–808.
- Twohy, C., A. J. Schanot, and W. A. Cooper: 1997, Measurement of condensed water content in liquid and ice clouds using an airborne counterflow virtual impactor. *J. Atmos. Ocean. Tech.*, **14**, 197–202.
- Valenzuela, G. R.: 1978, Theories for the interaction of electromagnetic and oceanic waves: A review. *Bound.-Layer Meteor.*, **13**, 61–85.
- Vanek, M. D., I. G. Nolt, N. D. Tappan, P. A. R. Ade, F. Gannaway, C. Lee, P. A. Hamilton, K. F. Evans, J. Davis, and S. Predko: 2001, Far infrared sensor for cirrus (FIRSC): An aircraft-based FTS to measure the earth radiance spectrum. *Appl. Optics*, **40**, 2169–2176.
- Wang, J. R., G. Liu, J. D. Spinhirne, P. Racette, and W. D. Hart: 2001, Observations and retrievals of cirrus cloud parameters using multichannel millimeter-wave radiometric measurements. *J. Geophys. Res.*, **106(D14)**, 15,251–15,263.
- Wang, J. R., P. Racette, J. D. Spinhirne, K. F. Evans, and W. D. Hart: 1998, Observations of cirrus clouds with airborne MIR, CLS, and MAS. *Geophys. Res. Letters*, **25(8)**, 1145–1148.

Weng, F. and N. C. Grody: 2000, Retrieval of ice cloud parameters using a microwave imaging radiometer. *J. Atmos. Sci.*, **57**, 1069–1081.

Wielicki, B. A., R. D. Cess, M. D. King, D. A. Randall, and E. F. Harrison: 1995, Mission to Planet Earth: Role of clouds and radiation in climate. *Bull. Amer. Meteor. Soc.*, **76**, 2125–2153.